J. Fluid Mech. (2005), *vol.* 545, *pp.* 339–372.
doi:10.1017/S0022112005006932 Printed in the United Kingdom

Mixing and dissipation in particle-driven gravity currents

By F. NECKER[1], C. HÄRTEL[1], L. KLEISER[1] AND E. MEIBURG[2]

[1]ETH, Institute of Fluid Dynamics, ETH Zentrum, CH-8092 Zürich, Switzerland
[2]Department of Mechanical and Environmental Engineering, University of California at Santa Barbara, Santa Barbara, CA 93106, USA

(Received 29 April 2002 and in revised form 3 May 2005)

Results are presented from a high-resolution computational study of particle-driven gravity currents in a plane channel. The investigation was conducted in order to obtain better insight into the energy budget and the mixing behaviour of such flows. Two- and three-dimensional simulations are discussed, and the effects of different factors influencing the flow are examined in detail. Among these are the aspect ratio of the initial suspension reservoir, the settling speed of the particles, and the initial level of turbulence in the suspension. While most of the study is concerned with the lock-exchange configuration, where the initial height of the suspension layer is equal to the height of the channel, part of the analysis is also done for a deeply submerged case. Here, the suspension layer is only one-tenth of the full channel height. Concerning the energy budget, a careful analysis is undertaken of dissipative losses in the flow. Dissipative losses arising from the macroscopic fluid motion are distinguished from those due to the microscopic flow around each sedimenting particle. It is found that over a large range of settling velocities and suspension reservoir aspect ratios, sedimentation accounts for roughly half of all dissipative losses. The analysis of the mixing behaviour of the flow concentrates on the mixing between interstitial and ambient fluid, which are taken to be of identical density. The former is assumed to carry a passive contaminant, whose dispersion with time is analysed qualitatively and quantitatively by means of Lagrangian markers. The simulations show the mixing between interstitial and ambient fluid to be more intense for larger values of the particle settling velocity. Finally, the question is addressed of whether or not initial turbulence in the suspension may exert a significant effect on the flow evolution. To this end, results from three simulations with widely different levels of initial kinetic energy are compared. While the initial turbulence level strongly affects the mixing within the current, it has only a small influence on the front velocity and the overall sedimentation rate.

1. Introduction

Gravity currents, which form when a heavier fluid propagates into a lighter one, are common in many environmental and engineering applications (see e.g. Simpson 1997). Particle-driven gravity currents are a special class of gravity currents, as in this case when the density difference is caused by a differential loading with suspended particles. Typical examples of particle-driven gravity currents are turbidity currents in oceans or lakes, which play an important role, for example, in erosion processes

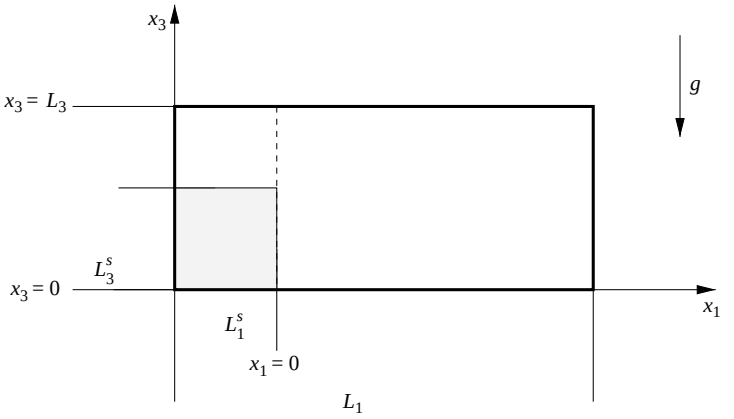

FIGURE 1. Sketch of the initial set-up of the simulations in a plane channel of length L_1, width L_2 and height L_3 (gravity acts in the vertical direction). Initially, a subvolume of the channel (length L_1^s, width $L_2^s = L_2$, height L_3^s) is filled with particle-laden fluid. The remaining part of the channel contains clear fluid, which is separated from the suspension by a vertical splitter plate located at $x_1 = 0$.

as well as in the transport of sediment (Huppert 1986; Parker, Fukushima & Pantin 1986; Middleton 1993; Dade & Huppert 1994; Kneller & Buckee 2000).

From a practical point of view, being able to predict both speed and run-out length of a particle-driven gravity current is of great interest. For such predictions, often simplified integral models or theoretical approaches based on shallow-water theory are employed (Bonnecaze, Huppert & Lister 1993; Dade & Huppert 1995; Gladstone & Woods 2000; Hogg, Ungarish & Huppert 2000; Ungarish & Huppert 2000). The empirical input required for validation of these models to a large extent stems from laboratory experiments (cf. Rottman & Simpson 1983; Altinakar, Graf & Hopfinger 1990; Bonnecaze *et al.* 1993; de Rooij & Dalziel 1998) in which global flow features such as the speed or height of propagating fronts are studied in prototype configurations. However, while the overall shape of the current and the speed of propagation are relatively easily monitored, velocity and concentration fields within the front are difficult to measure accurately in the laboratory. This is mainly because the application of advanced optical techniques is complicated in particle-laden flows. Here, high-resolution numerical simulations can help to provide the missing insight required to close some of the gaps in knowledge. For density-driven gravity currents, the first high-resolution simulations were presented by Härtel *et al.* (2000*a*, *b*). Particle-driven gravity currents were tackled by Necker *et al.* (2002).

Following up on that work, we present in this paper a numerical simulation study of several issues which are fundamental to the motion of gravity currents, but which have not been examined in detail in previous work. As a generic configuration, we will consider particle-driven fronts in a plane channel which is filled with particulate suspension and clear fluid. A principle sketch of the initial set-up is given in figure 1. Most of our analysis will be concerned with a lock-exchange situation, where the height of the suspension layer is identical to the height of the channel. For this case, the length of the reservoir is varied in order to examine the effect of the aspect ratio of the suspension volume. Moreover, a simulation is made for a reservoir of height much smaller than the channel height, in order to highlight differences and similarities between the lock-exchange configuration and a deeply submerged particulate gravity

current. Both three-dimensional and two-dimensional simulations are performed, and, at times, reference to density-driven flows is made for direct comparison of the results.

The first issue we wish to address in the present study relates to the energy bugdet of the flow. Here, we will focus on the overall balance between potential energy, kinetic energy and dissipative losses. The relevance of this issue becomes clear from the fact that gravity-induced dispersion in essence means conversion of potential energy into kinetic energy of fluid motion. The fluid motion in turn is subject to viscous friction which impedes the flow. In particle-driven gravity currents, the situation is further complicated by the fact that sedimentation of the suspended matter acts as an additional sink of energy. Although this energy loss does not directly counteract the fluid motion, it reduces continuously the driving potential of the flow. This phenomenon is absent in purely density-driven gravity currents, and it makes particulate fronts come to rest after a certain run-out length. Clearly, how far a front will spread depends directly on how much of the initially available potential energy remains available for inducing large-scale fluid motion. This in turn depends on both the particle characteristics and the initial setting of the flow. In the present paper, we will examine these dependencies by considering lock-exchange flows which differ with respect to the particle settling speeds, and which evolve from rectangular suspension reservoirs of different aspect ratios.

The second issue addressed here is the mixing behaviour of particulate gravity currents. Entrainment of – and mixing with – ambient fluid has been studied in some detail for density-driven flows (cf. Beghin, Hopfinger & Britter 1981; Thomas & Simpson 1985; García & Parsons 1996; Hallworth *et al.* 1996), but much less is known about particulate flows in this respect. Again, compared with the density-driven case, particle-driven flows feature additional complications due to particle settling, which makes it necessary to distinguish between ambient fluid, particulate matter and interstitial fluid (i.e. the fluid that initially carries the particles). For simplicity, we will restrict our attention to cases in which the interstitial fluid is of the same density as the ambient fluid, although the case of different densities can be tackled as well with the simulation approach we adopt (for experimental work in this field, see e.g. Sparks *et al.* 1993; Maxworthy 1999). Special attention will be devoted here to the long-term evolution of the mixing between ambient fluid and interstitial fluid. This is of interest, for example, if the latter is contaminated with a passive substance, which can continue to spread in the flow domain for times much longer than the finite lifetime of the particulate front. The dispersion of the contaminants will be monitored and quantified by means of passive marker particles that are tracked in the flow field.

Finally, the third point to be investigated here refers to the role that the initial level of turbulence in the suspension reservoir plays for the flow development. While the ambient fluid may be almost quiescent in many applications, the suspension is often in turbulent motion at the outset of a gravity-driven particulate flow. Specifically, our study is motivated by the fact that the suspension is normally in a highly turbulent state in laboratory experiments on lock-exchange particulate gravity currents, where the fluid is stirred before the release in order to have all particles evenly distributed in the suspension (see e.g. Gladstone, Phillips & Sparks 1998). To date, simplified dispersion models of particulate gravity currents do not take the initial flow state within the suspension into account; however, as of now, there is no evidence that this flow state can indeed be safely neglected.

Before we turn to the discussion of our computational results, the governing equations together with the numerical approach adopted are briefly outlined in

the following section. Subsequently, the general structure of particulate fronts is discussed, as these are obtained from three-dimensional simulations of lock-exchange and deeply-submerged flows. In § 4, we will examine the energy budget of the flow, and discuss in detail the losses due to particle sedimentation and viscous dissipation in the velocity field. Section 5 is then devoted to the qualitative and quantitative analysis of the mixing of ambient fluid and interstitial fluid. Finally, the role of initial turbulence will be discussed in § 6, before we summarize our main findings in § 7.

2. Numerical approach

We concentrate on dilute incompressible fluid flows laden with small monodisperse particles whose density $\tilde{\rho}_p$ is significantly higher than the constant density of the fluid $\tilde{\rho}$ (a tilde denotes a dimensional quantity here). The dispersed phase is assumed to be sufficiently dilute to have a negligible volume fraction $\tilde{c} \ll 1$, so that the two-way coupling between the fluid and the particles will be caused primarily through the momentum equation, and the effect of the particles can be neglected in the continuity equation. The small volume fraction of the dispersed particles furthermore allows us to neglect interactions among the particles, such as hindered settling. In addition, the particles are assumed to have an aerodynamic response time that is much smaller than typical fluid flow time scales. Hence, the particle velocity is given by the sum of the fluid velocity and the constant settling velocity. Since the fluid velocity field is divergence free and the settling velocity is constant, the particle velocity field is solenoidal as well, and particles will not accumulate anywhere in the flow field.

Under the above conditions of negligible particle inertia and volume fraction, the mathematical description of the particulate phase is most easily accomplished by an Eulerian transport equation for the local particle number density. In order to describe the motion of the fluid phase, the incompressible Navier–Stokes equations for a constant-density fluid are employed, augmented by a forcing term that accounts for two-way coupling, i.e. for the force that the particles exert on the carrier fluid.

In order to render the equations dimensionless, we use $\tilde{L}_3^s/2$ as the characteristic length scale (see figure 1). As the characteristic velocity scale, the buoyancy velocity $\tilde{u}_b$ is employed

$$\tilde{u}_b = \sqrt{\tilde{g}' \tilde{L}_3^s/2}, \tag{2.1}$$

where $\tilde{g}'$ is the reduced acceleration due to gravity

$$\tilde{g}' = \frac{\pi(\tilde{\rho}_p - \tilde{\rho})\tilde{c}_0 \tilde{d}_p^3}{6\tilde{\rho}} \tilde{g} \tag{2.2}$$

and $\tilde{c}_0$ is the initial (uniform) particle concentration in the suspension. In dimensionless form the governing equations thus read

$$\frac{\partial u_l}{\partial x_l} = 0, \tag{2.3}$$

$$\frac{\partial u_i}{\partial t} + u_l \frac{\partial u_i}{\partial x_l} = -\frac{\partial p}{\partial x_i} + \frac{1}{\sqrt{Gr}} \frac{\partial^2 u_i}{\partial x_l \partial x_l} + c e_i^g, \tag{2.4}$$

$$\frac{\partial c}{\partial t} + \left(u_l + u_s e_l^g\right) \frac{\partial c}{\partial x_l} = \frac{1}{\sqrt{Sc^2 Gr}} \frac{\partial^2 c}{\partial x_l \partial x_l}, \tag{2.5}$$

where u_i is the velocity vector and $c = \tilde{c}/\tilde{c}_0$ the dimensionless particle concentration. $\boldsymbol{e}^g = (0, 0, -1)$ is the vector pointing in the direction of gravity and p is the

dimensionless pressure $p = \tilde{p}/\tilde{\rho}\tilde{u}_b^2$. The diffusion term on the right-hand side of (2.5), which, as explained below, is kept small in the numerical simulations, has been included primarily in order to avoid the formation of discontinuities in the particle concentration field. However, there is a physical motivation as well, as this small amount of diffusion can mimic the fact that sharp concentration interfaces in particulate suspensions usually spread with time. This spreading may be caused by such effects as the hydrodynamic diffusion of particles, or slight imperfections in the monodispersivity of the suspension. The details of this diffusion-like spreading of the interface depend on the situation considered, and we have not attempted here to match the diffusion term to a particular experiment or application.

A few comments are in order regarding the derivation of the above momentum equation. We start from a general form that accounts for volume fraction effects in the momentum equation for the suspension

$$[(1-\tilde{c})\tilde{\rho} + \tilde{c}\tilde{\rho}_p]\left(\frac{\partial \tilde{u}_i}{\partial \tilde{t}} + \tilde{u}_l \frac{\partial \tilde{u}_i}{\partial \tilde{x}_l}\right) = -\frac{\partial \tilde{p}}{\partial \tilde{x}_i} + \tilde{\mu}\frac{\partial^2 \tilde{u}_i}{\partial \tilde{x}_l \partial \tilde{x}_l} + \tilde{c}(\tilde{\rho}_p - \tilde{\rho})\tilde{g}_i. \tag{2.6}$$

Slightly rewritten, we obtain

$$\tilde{\rho}\left(1 + \tilde{c}\frac{\tilde{\rho}_p - \tilde{\rho}}{\tilde{\rho}}\right)\left(\frac{\partial \tilde{u}_i}{\partial \tilde{t}} + \tilde{u}_l \frac{\partial \tilde{u}_i}{\partial \tilde{x}_l}\right) = -\frac{\partial \tilde{p}}{\partial \tilde{x}_i} + \tilde{\mu}\frac{\partial^2 \tilde{u}_i}{\partial \tilde{x}_l \partial \tilde{x}_l} + \tilde{\rho}\tilde{c}\frac{\tilde{\rho}_p - \tilde{\rho}}{\tilde{\rho}}\tilde{g}_i. \tag{2.7}$$

Note that for systems of interest in the present investigation, such as sand in water, the quantity $(\tilde{\rho}_p - \tilde{\rho})/\tilde{\rho}$ is $O(1)$, so that $\tilde{c}(\tilde{\rho}_p - \tilde{\rho})/\tilde{\rho} \ll 1$. Hence, the increased density component of the acceleration term on the left-hand side is much smaller than the leading-order constant-density component, and we can neglect it. This corresponds to the frequently applied Boussinesq approximation for flows with small fluid density variations.

It may be of interest to compare the relative magnitudes of this neglected density increase term and the viscous term, which will be retained in the simulation. Clearly, acceleration scales as

$$\tilde{u}_b^2/\tilde{L}_3^s \sim \tilde{g}' = \tilde{c}\frac{\tilde{\rho}_p - \tilde{\rho}}{\tilde{\rho}}\tilde{g}, \tag{2.8}$$

so that the neglected density increase component of the acceleration term scales as

$$\tilde{\rho}\tilde{c}^2\left(\frac{\tilde{\rho}_p - \tilde{\rho}}{\tilde{\rho}}\right)^2\tilde{g}. \tag{2.9}$$

Regarding the viscous term, a formal analysis with

$$\tilde{\mu}\frac{\partial^2 \tilde{u}_i}{\partial \tilde{x}_l \partial \tilde{x}_l} \sim \tilde{\mu}\frac{\tilde{u}_b}{\tilde{L}_3^{s2}}, \tag{2.10}$$

would suggest that for the neglected density increase term to be much smaller than the viscous term, the following must hold,

$$\tilde{c}\frac{\tilde{\rho}_p - \tilde{\rho}}{\tilde{\rho}} \ll \frac{1}{\sqrt{Gr}}. \tag{2.11}$$

However, this conclusion is misleading, since there is significant shear in the boundary and mixing layers of the flow, where velocity variations on the scale of $\tilde{u}_b$ occur over length scales much smaller than $\tilde{L}_3^s$. Hence, accumulated over space and time, this term can make a contribution that is larger than suggested by the above scaling

argument. Consequently, we will establish the order of magnitude of the viscous term *a posteriori* (cf. below).

One way to perform this *a posteriori* check is to multiply the momentum equation by $\tilde{u}_i$ in order to obtain the kinetic energy equation, and to compare the volume and time integrals of the individual terms in this equation. This will be done below, and it will show that the dissipated energy is of the same order as the kinetic energy associated with the constant-density term. From this we can conclude *a posteriori* that the neglected variable-density term is much smaller than the viscous term. This justifies neglecting the variable-density component of the Lagrangian acceleration term, while retaining the viscous term.

Independently of the above argument, the viscous term, of course, always has to be retained in a direct numerical simulation of turbulent flow, as it determines the size of the smallest scales in the flow.

Three dimensionless parameters appear in (2.3)–(2.5), namely the Grashof number Gr, the Schmidt number Sc, and the dimensionless settling velocity of the particles u_s,

$$Gr = \left(\frac{\tilde{u}_b \tilde{L}_3^s / 2}{\tilde{\nu}} \right)^2, \tag{2.12}$$

$$Sc = \frac{\tilde{\nu}}{\tilde{\kappa}}, \tag{2.13}$$

$$u_s = \frac{\tilde{u}_s}{\tilde{u}_b}, \tag{2.14}$$

with $\tilde{\nu}$ being the kinematic viscosity of the fluid, and $\tilde{\kappa}$ indicating the diffusivity of the particle concentration field. The Grashof number represents the ratio of buoyancy forces and viscous forces in the fluid. The Schmidt number is the ratio of the diffusivities in the velocity and the concentration field, and it is generally set to unity here. In general, there may be many reasons why the particle path may differ slightly from the path of a fluid element. Among these are, for example, particle geometry, particle inertia and Brownian motion. These microscopic effects, which can vary substantially from one application to another, are lumped together into an effective particle diffusion for the purpose of the present simulations. In order to obtain information on the influence of the Schmidt number in these simulations, we carried out a number of test calculations for different values of Sc. We found that the resulting flow is nearly independent of Sc, as long as Sc is not much smaller than one. For this reason, setting $Sc = 1$ in the current simulations represents an assumption that does not limit the general applicability of the results. Finally, the dimensionless velocity u_s quantifies the relative importance of particle sedimentation. It is computed from the buoyancy velocity and the settling speed $\tilde{u}_s$. The latter can be determined by balancing the gravitational forces with the Stokes drag of a single free-falling sphere. The larger the value of u_s, the earlier the flow will deviate from a density-driven gravity current, which corresponds to the case $u_s = 0$.

The numerical integration of the governing equations in the flow domain sketched in figure 1 is accomplished by a numerical scheme based on spectral and spectral-element discretizations in space, along with finite differences in time. A detailed description of the computational technique, along with a validation study and comparisons with experimental data, can be found in Härtel *et al.* (1997, 2000*a*) and Necker *et al.* (2002). In x_1 and x_2, the boundaries of the flow domain are treated as symmetry planes for both velocity and concentration. At the top and bottom of the computational domain, no-slip walls are prescribed in the simulations, i.e. $u_i = 0$. For the concentration field,

we use a no-flux boundary condition at the top boundary, which ensures that no particulate matter is transported across that plane. This is achieved by imposing

$$u_s c - \frac{1}{\sqrt{Sc^2 Gr}} \frac{\partial c}{\partial x_3} = 0 \quad \text{at} \quad x_3 = L_3. \tag{2.15}$$

On the other hand, at the bottom of the channel, it is assumed that the particles leave the flow owing to sedimentation. Numerically, this is accomplished by an 'outflow' boundary condition, i.e. a convective boundary condition with the settling speed taken as the characteristic velocity. Thus, we prescribe at the lower boundary

$$\frac{\partial c}{\partial t} = u_s \frac{\partial c}{\partial x_3} \quad \text{at} \quad x_3 = 0. \tag{2.16}$$

Clearly, the applicability of this approach requires that no resuspension of particles back into the flow occurs. Over the range of Grashof numbers considered in this investigation, appreciable resuspension of particles is unlikely to occur (cf. Necker *et al.* 2002).

3. Structure of the front

Before we turn to a detailed discussion of the energy budget and the mixing properties of the flow, we will give an impression of the structure of a particle-driven front as obtained from the three-dimensional simulations. In figures 2(*a*) and 2(*b*), surfaces of constant particle concentration are depicted for a lock-exchange flow at a Grashof number of 5×10^6 and a dimensionless settling velocity of $u_s = 0.02$. These values are typical for a range of more recent experiments (see e.g. Bonnecaze *et al.* 1993; de Rooij & Dalziel 1998). The flow domain in the simulation has a lateral size of $L_2 = 2$. In the initial stage of the flow, the length L_1 was set to $L_1 = 18$, and for the numerical discretization $N_1 \times N_2 \times N_3 = 1440 \times 200 \times 221$ grid points were used. The initial length of the domain is about 2 units more than the final run-out length of the front, which ensures that the propagating current is not affected by the end boundary in the downstream direction (cf. Härtel 2001). For the study of mixing in the later stages of the flow, however, the length of the channel was successively extended to $L_1 = 23$. Initially, the suspension part was confined to a subvolume of aspect ratio $L_1^s/L_3^s = 1/2$, which is identical to the initial set-up used in the experiments of Bonnecaze *et al.* (1993), Dade & Huppert (1995), Gladstone *et al.* (1998) and Hallworth *et al.* (1996). As initial condition, fluid at rest was prescribed, but in order to enhance the breakdown of the flow into a three-dimensional state after the release, weak turbulent disturbances in the velocity field were superimposed in the neighbourhood of the interface at time $t = 0$. This turbulence field has kinetic energy of about 0.5 % of the initial potential energy and was obtained from a separate simulation of decaying turbulence conducted in a very short computational domain of length $L_1 = 0.2$.

Upon release of the suspension, a front forms, which travels along the lower wall under the influence of gravity (cf. figure 2*b*). Readily seen from the figure is the pronounced head of the front, which is of particular interest as far as the mixing of ambient fluid into the front is concerned (cf. Hallworth *et al.* 1996). Once the front is fully developed, the head features the characteristic lobe-and-cleft instability, which can be better seen in the close-up in figure 2(*c*). The lobe-and-cleft structure is accompanied by an intense three-dimensionality in the flow (cf. Simpson 1972; Härtel *et al.* 2000*b*) which leads to strong spanwise variations in the concentration field at the leading edge. Moreover, the concentration field underneath the current features

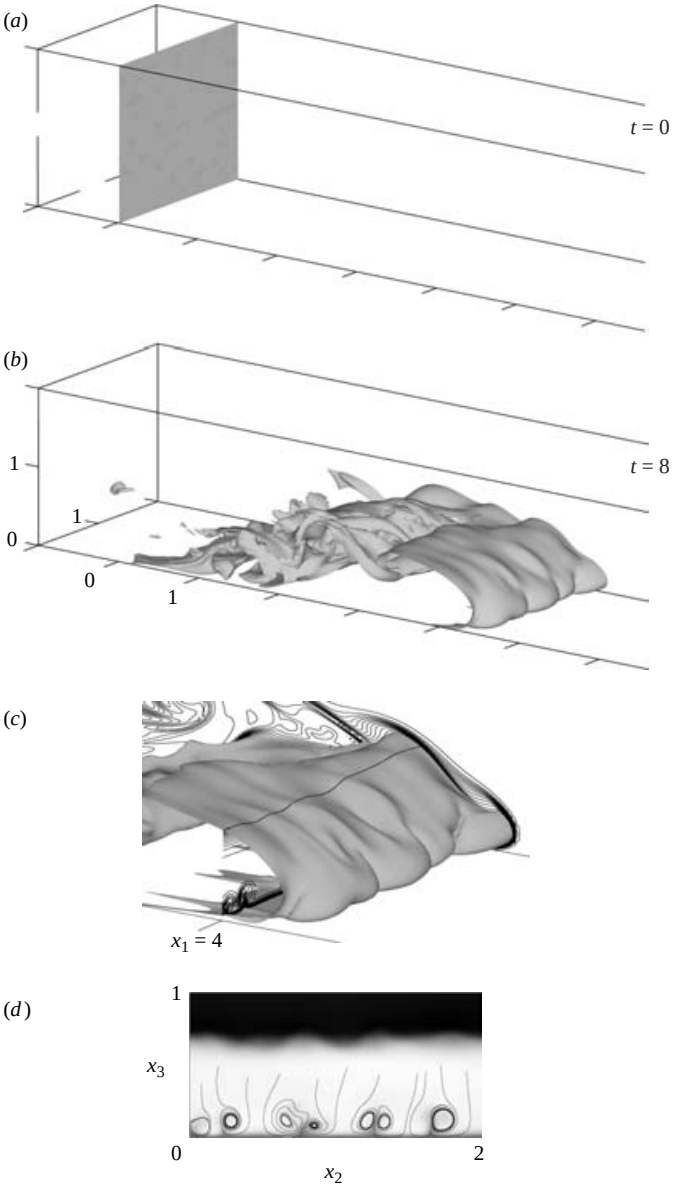

FIGURE 2. Structure of a particle-driven gravity current. Results obtained from a three-dimensional simulation with $Gr = 5 \times 10^6$ and $u_s = 0.02$. (*a*)–(*c*) Surfaces of concentration at $t = 0, t = 8$, and a close-up of the foremost part of the front at $t = 8$, respectively. In all cases, a concentration value of 0.5 is plotted. Also included in (*c*) are contours of concentration in the back plane, and in the (x_2, x_3)-plane at $x_1 = 4$. (*d*) Integral lines of the (u_2, u_3) vector field evaluated in the (x_2, x_3)-plane at $x_1 = 4$ and $t = 8$. The local values of streamwise velocity are indicated by a grey scale. Black, $u_1 = -0.38$; white, $u_1 = 0.65$.

a streaky structure. The flow field above these longitudinal streaks is characterized by pairs of counter-rotating vortices (see also Allen 1971), which are illustrated in figure 2(*d*) by means of sectional streamlines computed from the velocity components u_2 and u_3 in a selected (x_2, x_3)-plane. These longitudinal vortices enable the current to entrain the near-wall layer of light fluid that is overrun by the propagating head.

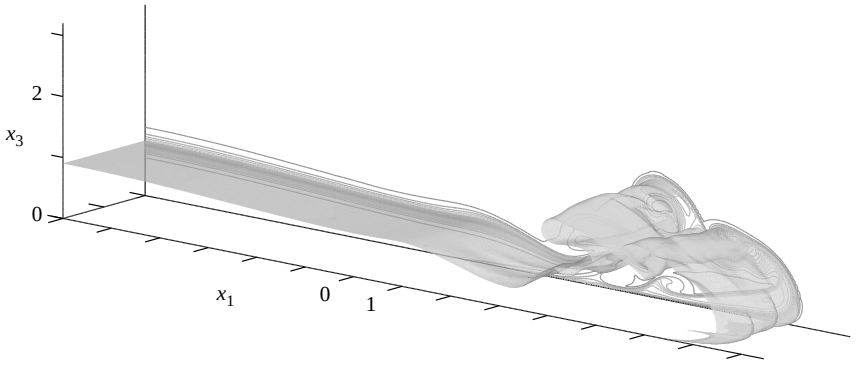

FIGURE 3. Structure of a deeply submerged particulate front for $Gr = 5 \times 10^6$ and $u_s = 0.02$, visualized by a surface of particle concentration at $t = 10$. Contour value set to 0.25.

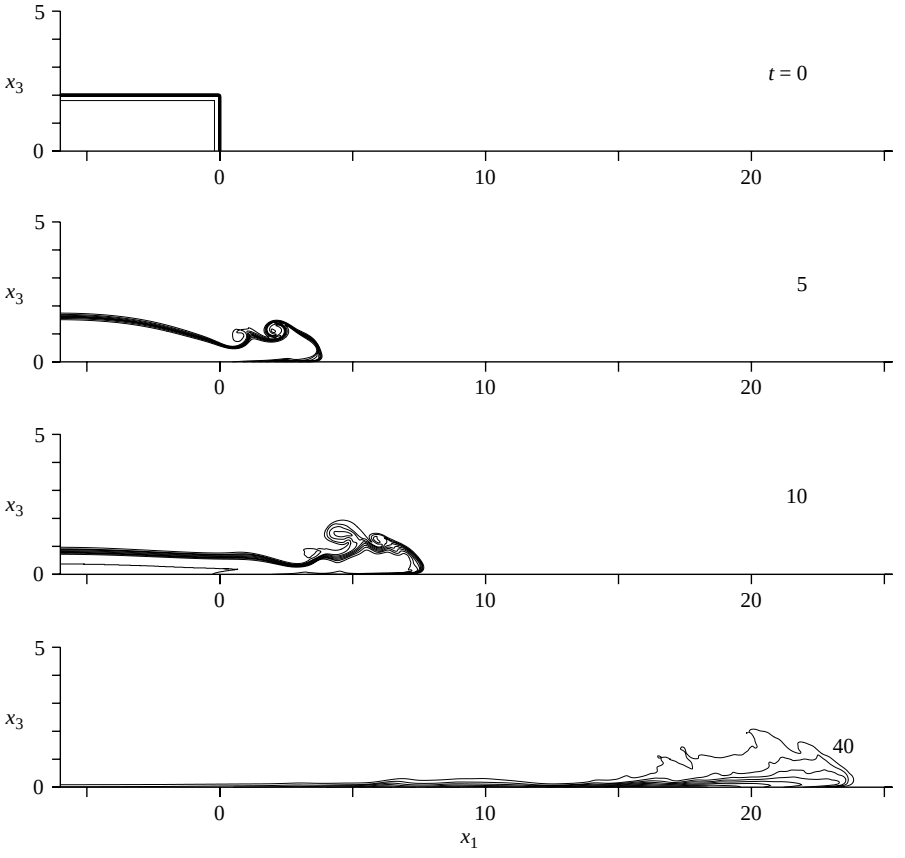

FIGURE 4. Contours of spanwise-averaged particle concentration. Same flow as in figure 3.

The typical features of a deeply submerged particulate gravity current can be recognized from figures 3 and 4. The flow develops from a reservoir of dimensionless size $L_1^s \times L_2^s \times L_3^s = 6 \times 2 \times 2$, and the height of the suspension layer is one-tenth the total channel height ($L_3 = 20$). Note that the length of the reservoir must be

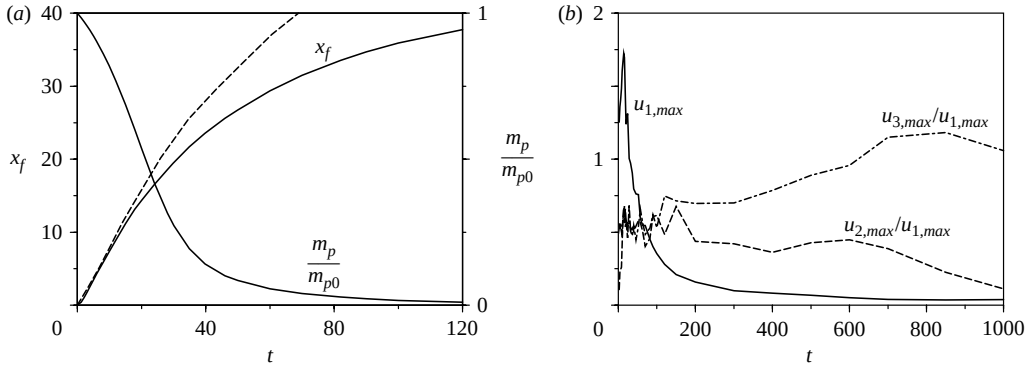

FIGURE 5. (*a*) Front position $x_f(t)$ and mass $m_p(t)$ of suspended particles (normalized with the initial mass m_{p0}) for $Gr = 5 \times 10^6$. Solid lines, results for the flow shown in figure 3 with $u_s = 0.02$; dashed line, two-dimensional result for density-driven gravity current. (*b*) Temporal evolution of maximum streamwise velocity $u_{1,max}$ (solid line). The dashed and dot-dashed lines denote, respectively, the maximum spanwise and vertical velocity $u_{2,max}$ and $u_{3,max}$, normalized by $u_{1,max}$.

several times its height in order to capture a typical feature of a deeply submerged current, namely sub- and supercritical flow state to the left and right of the initial front position, respectively. The Grashof number of the flow is 1.25×10^6, and the settling velocity is maintained at $u_s = 0.02$. At the foremost part of the front, a similar structure develops as in the lock-exchange case, with strong interfacial vortices and a lobe-and-cleft instability acting at the leading edge. However, the fluid within the reservoir to the left of the initial vertical interface flows out smoothly without mixing with the ambient. This behaviour is also observed in laboratory experiments on deeply submerged density-driven fronts (see Rottman & Simpson 1983). The concentration fields in figure 4 indicate that the front propagates at constant speed during the early flow stages. To make this more evident, the temporal evolution of the front position x_f is plotted in figure 5(*a*), together with the time history of the mass of suspended material. Here, and in what follows, m_p is defined as the volume integral of non-dimensional particle concentration, i.e.

$$m_p(t) = \int_\Omega c \, \mathrm{d}V. \tag{3.1}$$

It can be seen from figure 5 that the front speed $u_f = \mathrm{d}x_f/\mathrm{d}t$ is constant initially, taking a value of $u_f \approx 0.78$. This is clearly smaller than the maximum streamwise velocity which is found within the front (cf. figure 5*b*). After about $t = 20$, when some 50 % of all particles have settled, the front speed continuously decays. Note that this is also the time when the speed of the particulate front starts to deviate more strongly from the speed of a density-driven gravity current. Eventually, the front comes to rest at a run-out length of about $x_f = 45$.

Figure 6 gives the time history of the sedimentation rate $\dot{m}_s$ for the deeply submerged flow, which is defined here as the time derivative of the total mass m_s of sedimented particles per unit span

$$\dot{m}_s(t) = \frac{\mathrm{d}m_s(t)}{\mathrm{d}t} = \frac{1}{L_2} \int_0^{L_1} \int_0^{L_2} c_w(x_1, x_2, t) u_s \, \mathrm{d}x_2 \, \mathrm{d}x_1, \tag{3.2}$$

where $c_w = c(x_3 = 0)$ is the concentration at the bottom wall. Taking a value of 0.12 at time $t = 0$, $\dot{m}_s$ steadily increases during the first time units. The reason is that, initially,

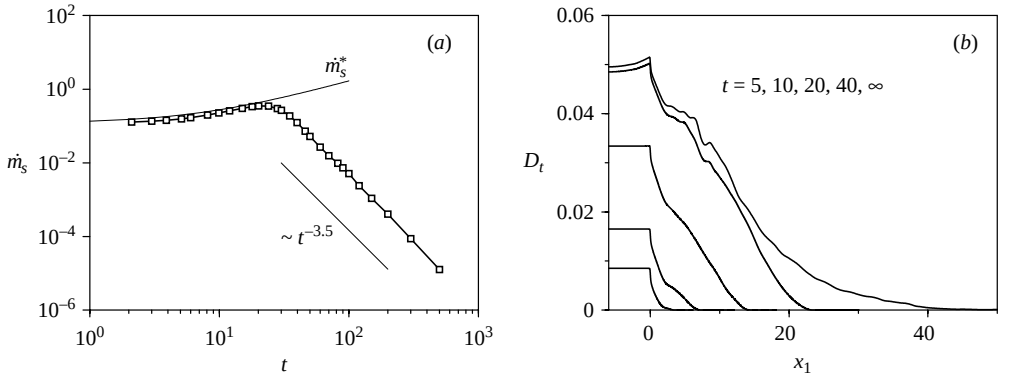

FIGURE 6. (*a*) Sedimentation rate $\dot{m}_s$ of the deeply submerged current at the bottom wall as function of time for $Gr = 5 \times 10^6$ and $u_s = 0.02$. Estimate $\dot{m}_s^*$ (see text) calculated with a front speed of $u_f = 0.78$. (*b*) Non-dimensional particle deposit D_t as function of x_1 for five different times. The curve for $t = \infty$ gives the final distribution after all particles have settled.

the current stretches out while remaining almost undiluted. An estimate $\dot{m}_s^*$ for the sedimentation rate at early times can therefore be obtained by setting $L_c = L_1^s + u_f t$ for the length L_c of the front. This yields

$$\dot{m}_s^*(t) = \left(L_1^s + u_f t\right) u_s. \tag{3.3}$$

The curve $\dot{m}_s^*$, calculated with $u_f = 0.78$, is included in figure 6, and close agreement with the actual sedimentation rate is observed until $t \approx 20$. Subsequently, an abrupt change in the sedimentation rate occurs. It leads to a rapid decay of $\dot{m}_s$ with time, following a power law $\dot{m}_s \sim t^n$ with $n = -3.5$. Note that for the lock-exchange flow a power law with a much smaller exponent of $n = -2.4$ is observed (see Necker *et al.* 2002). We remark here that the linear growth $\dot{m}_s^*$, observed during the first 20 time units, lends support to the concept of a 'laminar' settling process (see Ungarish & Huppert 1998) as opposed to a thorough turbulent mixing of the suspended matter across the front height. When laminar settling prevails, the particle density in the suspension remains essentially unchanged, (cf. figure 4) while the upper interface between suspension and clear fluid slowly drops in height. From the present data, we conclude that a laminar settling process is appropriate in the initial stage of a deeply submerged gravity current. On the other hand, we found no such behaviour in the lock-exchange simulations, especially when the initial lock length is relatively small.

The settling of particles produces a sediment layer at the bottom of the tank, which is non-uniform in the streamwise direction. This is shown in figure 6(*b*), where a mean deposit D_t per unit span (cf. Necker *et al.* 2002) is plotted. In the initial reservoir ($x_1 < 0$), the sediment layer grows almost linearly during the first 20 time units. After all particles have settled ($t \to \infty$), the largest values in D_t are encountered in this region. This is markedly different from what is found with lock-exchange flows, where a distinct maximum develops downstream of the initial lock (see Bonnecaze *et al.* 1993; Necker *et al.* 2002).

For deeply submerged particulate fronts, no experimental data are available for comparison. However, given the small differences in the front speed of particulate and density-driven currents during the first few time units, a comparison with the front speed measurements of Rottman & Simpson (1983) can be undertaken. From the present results, and the data presented in Necker *et al.* (2002), we find that for

the case $L_3/L_3^s = 10$, the front speed is 1.36 times the front speed of a lock-exchange current. This is in close agreement with the findings of Rottman & Simpson (1983), who report values between 1.32 and 1.45 for the same length ratio. The reason for choosing the ratio of front speeds here for comparison, rather than the absolute values of u_f, is that the front speed of gravity currents to some extent depends somewhat on Gr (see Härtel *et al.* 2000*a*), so that the influence of deep submersion should be evaluated for constant Gr. Since viscous effects are similar in lock-exchange flows and deeply submerged currents, Gr dependencies can be partially compensated for if the ratio of u_f is taken.

4. Energy budget of the flow

In essence, any gravity-driven flow can be understood as a conversion of potential energy into kinetic energy, i.e. fluid motion, which subsequently is dissipated into heat by viscous friction. In density-driven gravity currents, dissipation is caused by gradients in the macroscopic 'convective' velocity field only, but in particle-driven gravity currents, dissipative losses also occur in the microscopic Stokes flow around each particle. In order to examine the temporal evolution of the different energy components, the budget equations for the kinetic and potential energy must be considered. The equation for the time derivative of the kinetic energy of the fluid is obtained from multiplication of the momentum budget (2.4) by u_i, which yields

$$\frac{\mathrm{D}}{\mathrm{D}t}\left(\tfrac{1}{2}u_i u_i\right) = -\frac{\partial}{\partial x_i}(p u_i) + \frac{1}{\sqrt{Gr}}\frac{\partial}{\partial x_j}(s_{ij}u_i) - \frac{2}{\sqrt{Gr}}s_{ij}s_{ij} - u_3 c, \tag{4.1}$$

where $\mathrm{D}/\mathrm{D}t$ indicates the material derivative, and s_{ij} denotes the rate-of-strain tensor

$$s_{ij} = \frac{1}{2}\left(\frac{\partial u_i}{\partial x_j} + \frac{\partial u_j}{\partial x_i}\right). \tag{4.2}$$

Integration of (4.1) over the entire flow domain Ω gives an equation for the temporal evolution of the total kinetic energy k, which is the quantity we will consider here

$$\frac{\mathrm{d}k}{\mathrm{d}t} = -\int_\Omega \frac{2}{\sqrt{Gr}}s_{ij}s_{ij}\,\mathrm{d}V - \int_\Omega u_3 c\,\mathrm{d}V, \tag{4.3}$$

where

$$k(t) = \int_\Omega \tfrac{1}{2}u_i u_i\,\mathrm{d}V. \tag{4.4}$$

Note that the first two terms on the right-hand side of (4.1) are divergence terms which, in the present case, vanish after integration over Ω (see Necker *et al.* 2002). The validity of equation (4.3) for particulate flows requires that the slip between particles and flow is significant in the gravitational direction only, which is the case for the parameters considered in the present study. In more general situations, the energy budget will feature further source terms stemming from frictional forces between particles and carrier fluid in all spatial directions.

The potential energy in the system is obtained from the integral

$$E_p(t) = \int_\Omega c\ x_3\,\mathrm{d}V, \tag{4.5}$$

and its time derivative is given by

$$\frac{\mathrm{d}E_p}{\mathrm{d}t} = \int_\Omega \frac{\mathrm{D}(c\ x_3)}{\mathrm{D}t}\,\mathrm{d}V = \int_\Omega u_3 c\,\mathrm{d}V + \int_\Omega x_3 \frac{\mathrm{D}c}{\mathrm{D}t}\,\mathrm{d}V. \tag{4.6}$$

The second term on the right-hand side of (4.6) can be rewritten by means of the transport equation, (2.5). For simplicity, we neglect here the effects that diffusion in the concentration field has on the potential energy (see Winters *et al.* 1995 for a discussion of such effects), and thus arrive at the following equation for E_p:

$$\frac{\mathrm{d}}{\mathrm{d}t}E_p = \int_\Omega u_3 c\,\mathrm{d}V + \int_\Omega x_3 u_s \frac{\partial c}{\partial x_3}\,\mathrm{d}V. \tag{4.7}$$

Summing (4.3) and (4.7), and taking into account that no change in potential energy occurs due to transport across domain boundaries (see Necker *et al.* 2002), we find for $\mathrm{d}/\mathrm{d}t(k + E_p)$, i.e. for the change of total mechanical energy with time,

$$\frac{\mathrm{d}}{\mathrm{d}t}(k + E_p) = -\int_\Omega \frac{2}{\sqrt{Gr}} s_{ij}s_{ij}\,\mathrm{d}V - \int_\Omega u_s c\,\mathrm{d}V \tag{4.8}$$

$$= -\varepsilon - \varepsilon_s, \tag{4.9}$$

where

$$\varepsilon = \int_\Omega \frac{2}{\sqrt{Gr}} s_{ij}s_{ij}\,\mathrm{d}V, \tag{4.10}$$

$$\varepsilon_s = \int_\Omega u_s c\,\mathrm{d}V. \tag{4.11}$$

Note that with the present approach, the kinetic energy of the particulate phase does not show up in the equation of total energy. This is because we only consider flows where g' is much smaller than g, meaning that the mass of the particulate phase can be neglected in the overall balance of kinetic energy. The two integrals ε and ε_s represent the losses in mechanical energy due to macroscopic convective fluid motion and microscopic Stokes flow around particles, respectively. In order to evaluate the latter, only the concentration field and the settling speed u_s need be known. Since u_s is constant, and the volume integral of the particle concentration is identical to the instantaneous mass of suspended matter, ε_s can also be written as

$$\varepsilon_s(t) = u_s m_p(t). \tag{4.12}$$

Note that, with the continuous description of the particulate phase employed here, the fundamental difference between these two contributions to the total dissipation is readily recognized: while ε_s acts as a sink of potential energy, ε represents a sink of kinetic energy.

Integrating (4.9) with respect to time yields

$$k + E_p + E_d + E_s = \text{const.} = k_0 + E_{p0}, \tag{4.13}$$

with E_{p0} being the initial potential energy, k_0 the initial kinetic energy, and E_d and E_s the time integrals of the dissipation components, i.e.

$$E_d(t) = \int_0^t \varepsilon(\tau)\,\mathrm{d}\tau, \tag{4.14}$$

$$E_s(t) = \int_0^t \varepsilon_s(\tau)\,\mathrm{d}\tau = u_s \int_0^t m_p(\tau)\,\mathrm{d}\tau. \tag{4.15}$$

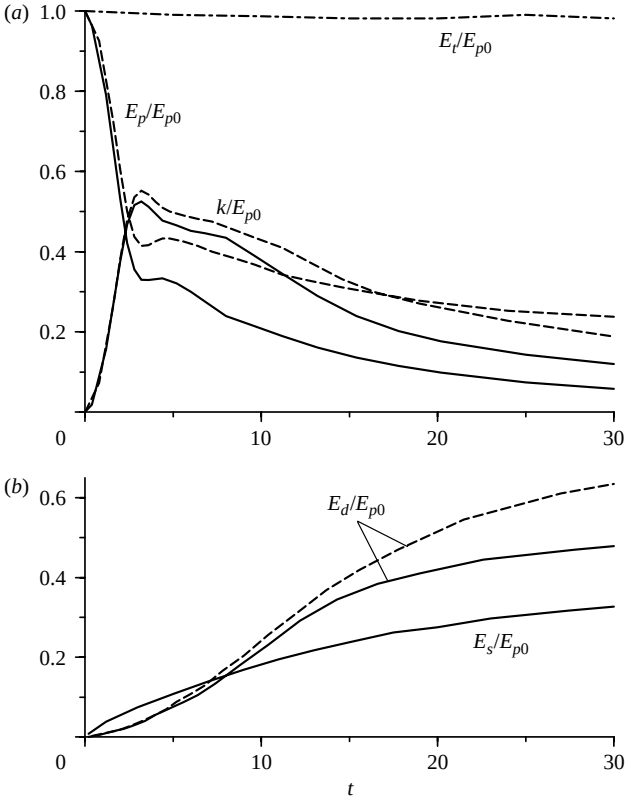

FIGURE 7. (*a*) Time history of potential energy E_p and kinetic energy k. (*b*) Time history of the dissipation components E_d and E_s. In both graphs, solid lines show the results for the lock-exchange flow depicted in figure 2; dashed lines show the results for a density-driven gravity current ($u_s = 0$) developing from the same initial set-up. The dot-dashed line in (*a*) gives the sum of E_p, k, E_d and E_s for the particle-driven flow. $Gr = 5 \times 10^6$.

The time history of the four terms on the left-hand side of (4.13), as obtained from the lock-exchange simulation shown in figure 2, is given in figure 7. To demonstrate that the effects of diffusion are indeed negligibly small, we have included the sum of all four terms which is denoted as E_t in the figure. It is seen that E_t is approximately constant, as required by overall energy conservation. We wish to point out that the slight variations of E_t are primarily caused by the limited accuracy of the first-order time integration scheme we employed for computing E_d and E_s from the instantaneous dissipation rates ε and ε_s, respectively.

As seen from figure 7, the first 2–3 time units of the flow are dominated by a fast conversion of potential energy into convective motion, which causes E_p to drop by almost 70 %. However, even though the potential energy continues to decrease during the further evolution of the flow, the kinetic energy, after having reached a maximum at $t \approx 5$, also starts to decay, reflecting the strongly increasing influence of dissipation. During the initial stages, the dissipative losses are clearly dominated by particle settling, but the macroscopic dissipation E_d overtakes E_s once the front reaches a fully turbulent state. It can be inferred from figure 7 that this causes a strong increase of the dissipation rate ε by a factor of about two. At times much later than those shown in the figure, both k and E_p tend to zero. On the other hand,

E_d and E_s approach final values that indicate, respectively, how much of the initially available potential energy was dissipated by macroscopic fluid motion, and how much was dissipated by settling. For the present case, we find that sedimentation accounts for a 'loss' of more than 40 % of E_{p0} which, hence, is not available for convective transport and turbulent mixing. This must be contrasted with a density-driven flow ($u_s = 0$), where no losses due to sedimentation occur.

For direct comparison of the energy budget of a particle-driven and a density-driven gravity current, we include in figure 7 the results for a density-driven flow with the same Grashof number and the identical initial set-up. Comparing the respective curves shows that the density-driven front exhibits larger values of potential energy throughout the simulation. Especially after $t = 10$, when the frontal speed of the particle-driven current becomes increasingly affected by sedimentation, relatively large differences are seen. The fact that E_p is generally smaller in the particle-driven case can be understood from the fact that sedimentation leads to an additional decrease in the elevation of the centre of mass of the dense phase. Figure 7 also reveals that, at identical non-dimensional times, a density-driven flow contains more kinetic energy than a particle-driven current. For example, at $t = 30$ the difference amounts to about 50 % of the kinetic energy in the density-driven flow. Note that these higher levels of kinetic energy are associated with larger values of the viscous dissipation E_d.

The amount of potential energy lost by sedimentation depends not only on the settling velocity, but also on the initial set-up. More specifically, it depends on the aspect ratio L_1^s/L_3^s of the initial reservoir filled with suspension. The influence of the aspect ratio is probably best understood from considering the case of a very long reservoir ($L_1^s/L_3^s \gg 1$), where the developing convective motion influences a relatively small fraction of the reservoir only, leaving a large portion of the channel almost unaffected for long times. Particle settling in that part of the reservoir where little or no macroscopic fluid motion exists, will then dominate the losses in potential energy. The potential energy loss of the particles due to the slumping of the front will be relatively small by comparison. In fact, in the limiting case of an infinitely long reservoir, E_s/E_{p0} tends to unity.

To illustrate how E_s depends on both the initial aspect ratio of the reservoir and the settling velocity, we have evaluated the final amount of the energy losses due to particle settling from a series of two-dimensional lock-exchange simulations. This final amount is denoted as E_s^* here, that is

$$E_s^* = \lim_{t\to\infty} E_s(t), \tag{4.16}$$

and the results are shown in figures 8 and 9. It is seen that, as expected, E_s^* increases with increasing aspect ratio, but the increase is rather weak. Also, E_s depends little on the settling velocity, at least between $u_s = 0.002$ and 0.02. Clearly, for sufficiently small values of the settling velocity, a particle-driven front closely resembles a density-driven front, which means that E_s^* has to approach zero for $u_s \to 0$. However, figures 8 and 9 demonstrate that already for a settling speed of the order of 10^{-2}, which is representative for many environmental applications (see e.g. Mohrig, Elverhøi & Parker 1999), the energy budget of a particle-driven gravity current differs fundamentally from the energy budget of a density-driven front. Even for settling speeds as small as 10^{-3}, a significant amount of potential energy will be lost owing to continued sedimentation.

Comparing figure 8 with the result obtained from the three-dimensional lock-exchange simulation reveals that two-dimensional simulations tend to overestimate E_s^*.

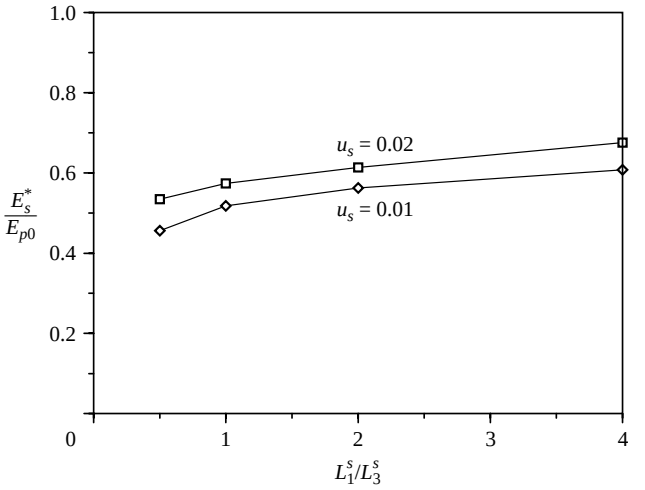

FIGURE 8. Final amount E_s^* of energy dissipated owing to particle settling (see (4.16)), as a function of the aspect ratio L_1^s/L_3^s of the reservoir initially filled with suspension. Results obtained from two-dimensional simulations for different settling velocities of $u_s = 0.01$ ($\diamond$) and $u_s = 0.02$ ($\square$), respectively. $Gr = 5 \times 10^6$.

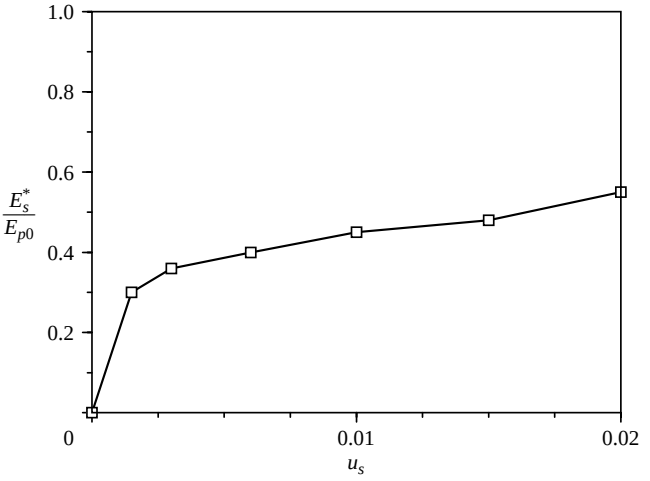

FIGURE 9. Final amount E_s^* of energy dissipated owing to particle settling (see (4.16)), as a function of the settling velocity u_s. Results obtained from two-dimensional simulations with an aspect ratio of the initial reservoir $L_1^s/L_3^s = 0.5$ and $Gr = 5 \times 10^6$.

For $u_s = 0.02$, E_s^*/E_{p0} is about 0.54 in the two-dimensional case, while a 25 % smaller value is computed from the three-dimensional simulation. Similarly, the respective result for the three-dimensional deeply-submerged flow is about 20 % smaller than corresponding result for the two-dimensional lock-exchange flow at $L_s^s/L_3^s = 3$ given in figure 8. This difference can be understood from the fact that two-dimensional flows develops large-scale vortices, which mix the flow in the vertical direction with little viscous dissipation. In this mixing, however, energy required to lift the particulate phase must be taken from the fluid motion, which causes enhanced sedimentation losses.

4.1. *Spatial distribution of dissipation*

The results presented previously show that, over a wide range of aspect ratios and settling speeds, about half of the initial potential energy in the system is dissipated by macroscopic fluid motion, while the Stokes flow around the sedimenting particles accounts for the rest of the dissipative losses. In theoretical models of particulate gravity currents, both dissipation components must be accounted for if the global energy balance is to be represented properly. Generally speaking, capturing E_s does not require the detailed flow field to be known, since the losses due to particle settling can be determined if the global sedimentation rate is correctly computed. On the other hand, the turbulent dissipation due to macroscopic velocity gradients, i.e. E_d, must be accounted for by additional closure assumptions, if the model does not resolve the flow field in its details. To derive and validate closures, knowledge of the spatial and temporal variation of the dissipation rate ε is required in order to help to identify both the regions where dissipation is most intense, and the flow structures which are associated with large dissipative losses. So far, no results on local or global dissipation rates have been available from the literature, because ε is virtually inaccessible to laboratory measurements.

An important mechanism of dissipation in gravity currents is wave breaking behind the head of the front (cf. Bonnecaze *et al.* 1993). In simplified models, the head loss is typically accounted for by adjusting the Froude number of the current, which is the boundary condition used for the velocity at the head (see e.g. Huppert & Simpson 1980), but dissipative losses downstream of the head are not considered. To see how the losses along the current compare with the loss at the head, we evaluated the integral over ε in (x_2, x_3)-planes for the lock-exchange simulation. This quantity is denoted as ε^{i23} here, i.e.

$$\varepsilon^{i23}(x_1) \equiv \int_0^{L_3} \int_0^{L_2} \varepsilon(x_1, x_2, x_3)\, \mathrm{d}x_2\, \mathrm{d}x_3. \tag{4.17}$$

The streamwise variation of ε^{i23} at time $t = 10$ is depicted in figure 10, together with contours of the spanwise averaged concentration field at the same time. Except for the rear part ($x_1 < 2$) where, after the reflection of the light fluid at the left wall, motion has largely ceased, dissipation is seen to occur over the full length of the current, with maximum values twice as high as near the head.

Usually, regions of large dissipation in the flow coincide with regions of large velocity gradients, which are encountered both in the mixing region in the interior of the channel and in the thin boundary layers. The relative importance of dissipative losses in these regions of the flow can be examined by integrating ε over length and width of the channel. This integral, denoted as ε^{i12}

$$\varepsilon^{i12}(x_3) \equiv \int_0^{L_2} \int_0^{L_1} \varepsilon(x_1, x_2, x_3)\, \mathrm{d}x_1\, \mathrm{d}x_2, \tag{4.18}$$

is depicted in figure 11, again for time $t = 10$. It is seen that the fluid motion at the interface between ambient fluid and suspension is responsible for the bulk of the dissipative losses, although the maximum of ε^{i12} is located in the boundary layer at the lower wall. To better quantify the contribution of the boundary layer to the total dissipation in the flow, we have integrated ε^{i12} with respect to x_3 and the respective integral $\varepsilon^{i12'}$

$$\varepsilon^{i12'}(x_3) \equiv \int_0^{x_3} \varepsilon^{i12}(x_3')\, \mathrm{d}x_3' \tag{4.19}$$

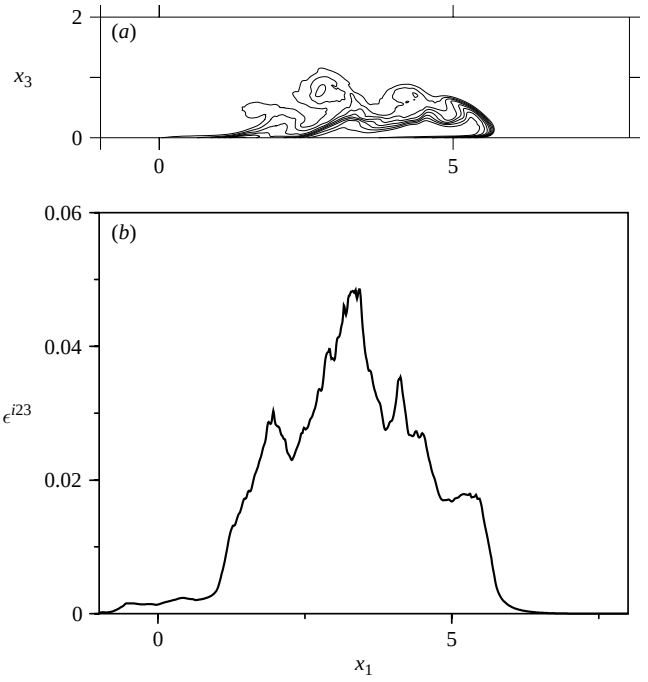

FIGURE 10. Streamwise distribution of viscous dissipation for $Gr = 5 \times 10^6$ and $u_s = 0.02$. Shown is the integral ε^{i23} over ε according to (4.17). (*a*) Contours of the spanwise-averaged particle concentration field. The results are obtained from the simulation shown in figure 2 at time $t = 10$, a time instant which features very high dissipation rates.

is included in figure 11. Although the boundary layer at the bottom is thin, it gives an appreciable contribution to the dissipative losses, as can be inferred from the rapid increase of $\varepsilon^{i12'}$ near $x_3 = 0$. The region $x_3 \in [0, 0.1]$, which accounts for only 5 % of the full channel height, contains approximately 15 % of the total dissipation. Clearly, these large values of dissipation in the near-wall zone are almost exclusively caused by the large gradients of u_1 in the normal direction x_3. In order to illustrate this, we have evaluated the contribution ε_{13}^{i12} of the component s_{13} of the rate-of-strain tensor to the integrated dissipation ε^{i12}

$$\varepsilon_{13}^{i12}(x_3) \equiv \int_0^{L_2} \int_0^{L_1} \frac{2}{\sqrt{Gr}} (s_{13}s_{13} + s_{31}s_{31}) \, \mathrm{d}x_1 \, \mathrm{d}x_2, \tag{4.20}$$

with the result included in figure 11. It is seen that ε_{13}^{i12} and ε^{i12} are virtually identical in the vicinity of $x_3 = 0$. Taking into account that $\partial u_3/\partial x_1$ is negligible here, this result demonstrates the dominant role that $\partial u_1/\partial x_3$ plays for the dissipation in the boundary layer.

5. Mixing of interstitial fluid and ambient fluid

Concerning mixing and dispersion in particulate flows, most of the work so far has focused on examining the dispersion of the particulate matter driving the flow. However, the spreading of the interstitial fluid, which is the fluid that initially carries the particles, becomes of interest too, if this fluid differs from the ambient fluid in density or composition. In the present study, we are dealing exclusively with the case

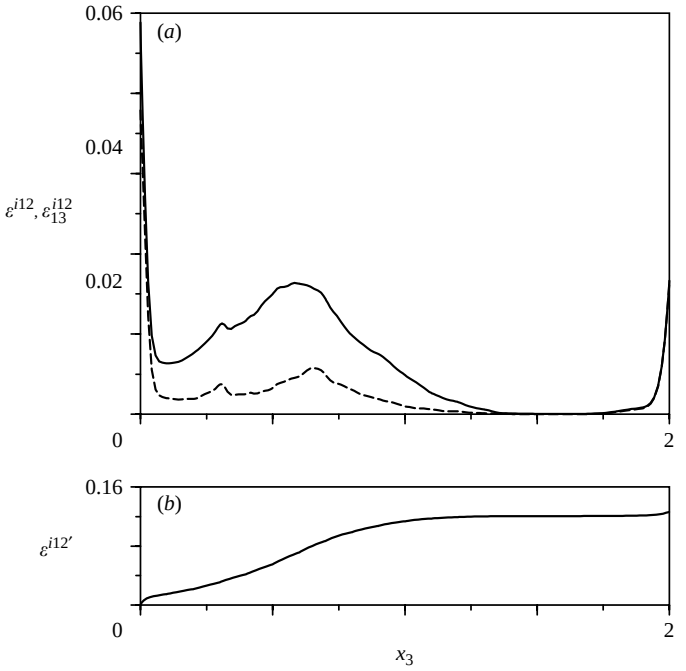

FIGURE 11. Vertical distribution of viscous dissipation for $Gr = 5 \times 10^6$ and $u_s = 0.02$. (*a*) Integrals ε^{i12} and ε^{i12}_{13} of ε according to (4.18) and (4.20) (solid and dashed line, respectively). (*b*) Integral $\varepsilon^{i12'}$ of ε according to (4.19). Same time instant as in figure 10.

in which the interstitial fluid is of the same density as the ambient fluid, but it is assumed to contain some passive contaminant. At early times, the dispersion of the interstitial fluid follows the spreading gravity current; however, owing to continual settling, particles and interstitial fluid segregate with time. While the particles collect at the bottom of the channel, the interstitial fluid together with the contaminant is being mixed with the ambient fluid by the vortical motion produced at the front. This mixing occurs to some extent already during the early stages of the flow, but it becomes more pronounced during the later flow development, when the stratification in the channel diminishes quickly. Note that even after all particles have settled out, i.e. after the motive force has completely disappeared, the flow has not yet come to rest. The kinetic energy available by that time will eventually decay by viscous dissipation, but it continues to mix interstitial fluid and ambient fluid for long times.

To investigate qualitatively and quantitatively the mixing process of ambient fluid and carrier fluid, a diffusion-free Lagrangian approach was chosen to follow the dispersion of the contaminant. To this end, 32 000 uniformly distributed passive markers were randomly added to the particle-laden fluid at time $t = 0$. In contrast to the heavy particles in the suspension, these markers do not affect the fluid motion. During the propagation of the gravity current, the markers are transported along the pathlines of the fluid, so that the distribution of the contaminant can be inferred from the marker field.

An impression of the progressive mixing of carrier fluid and ambient fluid in the lock-exchange flow shown in figure 2 can be gained from figure 12 where the distribution of markers is depicted by side views at selected times. At $t = 20$ and 40, the typical shape of a gravity current is still discernible from the markers, even though

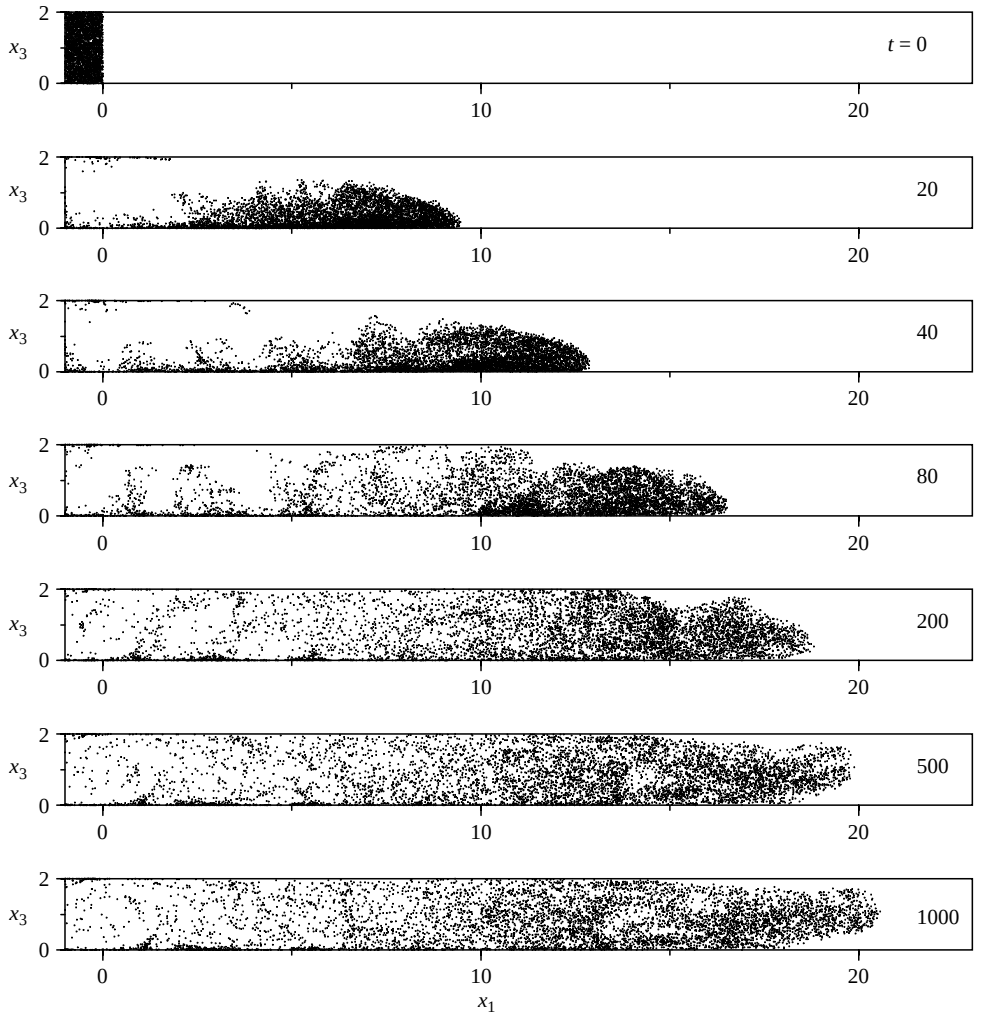

FIGURE 12. Dispersion of interstitial fluid in a particle-driven gravity current visualized by passive markers for $Gr = 5 \times 10^6$ and $u_s = 0.02$. Same flow as in figure 2.

at these times a significant amount of particles have already settled. Subsequently, the cloud of markers slowly spreads out in the vertical direction, indicating a thorough mixing of carrier and ambient fluid across the full channel height. As pointed out before, this mixing of carrier and ambient fluid is caused by the remaining fluid motion after complete sedimentation. For a quantitative assessment of this mixing process, a local concentration of the contaminant can be defined by means of the local number density of markers. A straightforward method to transform the distribution of discrete elements into a smooth concentration field is to count the markers located in an individual cell of the computational mesh, divide the number obtained by the cell volume and relate the result to the initial marker density in the suspension. While this approach is easily implemented, it gives unsatisfactory, highly intermittent results in regions where the markers are sparsely distributed. Therefore, we have applied a different method here, which is adopted from the way in which interpolation between discrete particles and a fixed mesh is accomplished in mixed Eulerian–Lagrangian

techniques (see e.g. Elghobashi & Truesdell 1993; Meiburg 1995; Maxey *et al.* 1997; Meiburg *et al.* 2000). The key idea is to define a region of influence surrounding each discrete element. This region of influence must be large enough to cover several mesh points of the underlying computational grid. Also, the region of influence must be adjusted to the distance between neighbouring markers in order to avoid the final concentration distribution becoming uneven and 'spotty'. In the present study, we defined the region of influence by using a shape function f_k, which is taken as a clipped Gaussian curve, i.e.

$$f_k(r_k) = \begin{cases} \dfrac{1}{(\sqrt{\pi}\sigma_k)^3} \exp\left[-\left(\dfrac{r_k}{\sigma_k}\right)^2\right] & \text{for} \quad r_k < 3\sigma_k, \\ 0 & \text{otherwise.} \end{cases} \tag{5.1}$$

In (5.1), σ_k is a measure of the width of the Gaussian, and $r_k = |\boldsymbol{x} - \boldsymbol{x}_k|$ denotes the distance between a point $\boldsymbol{x}$ and the instantaneous position $\boldsymbol{x}_k$ of marker k. The continuous marker concentration field $c_m(\boldsymbol{x})$ is then obtained by summing up the contributions of all M individual markers, i.e.

$$c_m(\boldsymbol{x}) = \frac{1}{M} \sum_{k=1}^{M} f_k(r_k). \tag{5.2}$$

Note that $c_m(\boldsymbol{x})$ should be defined such that the average marker concentration is unity within the reservoir at $t = 0$, which can be achieved by choosing σ_k properly. In the present study, the width of the Gaussian curve σ_k is calculated for each marker separately, and is taken to be the distance between the marker and its third nearest neighbour. However, to cope with cases in which a small number of markers are localized extremely close to each other, a lower limit for σ_k must be prescribed. In the present study, this lower limit is taken as the maximum side length Δ of the mesh cell surrounding a marker.

With the continuous marker concentration c_m, the mixing of the interstitial and ambient fluid can be quantified by computing the subvolume of the flow domain where c_m ranges between given bounds or where it exceeds a certain threshold value. The subvolume containing fluid with marker concentrations above a threshold $c_{m,\theta}$ will be denoted as $V_{m,\theta}$ here, and is computed from the following integral

$$V_{m,\theta} = \frac{1}{L_1^s * L_2^s * L_3^s} \int_{\Omega} \alpha \, \mathrm{d}V, \tag{5.3}$$

where

$$\alpha = 1, \quad c_m \geqslant c_{m,\theta},$$
$$\alpha = 0, \quad c_m < c_{m,\theta}.$$

$V_{m,\theta}$ is a measure for the increase in volume of the contaminated fluid, as defined by the threshold, which occurs due to entrainment of ambient fluid. By comparing results of $V_{m,\theta}$ for different $c_{m,\theta}$, it can be examined how homogeneously the carrier fluid is distributed within the volume in which mixing occurs. For perfect mixing over the channel (or part of it), c_m is constant in the mixed region, and $V_{m,\theta}$ is constant for $c_{m,\theta} \leqslant c_m$ and zero for $c_{m,\theta} > c_m$, respectively. This situation is encountered at $t = 0$ when the markers are evenly distributed within the initial suspension. Consequently, $V_{m,\theta}$ is unity for $0 \leqslant c_{m,\theta} \leqslant 1$ as can be seen from figure 13. In addition, figure 13 gives results for $V_{m,\theta}$ at four more time instants, which show that the regions with low concentrations of carrier fluid grow significantly with time. Moreover, the

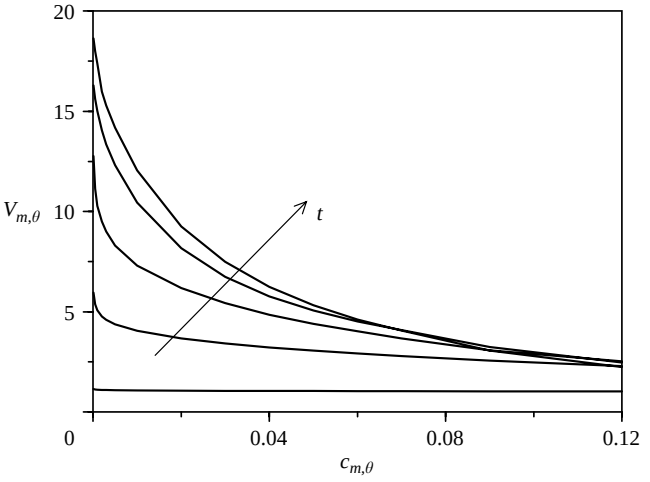

FIGURE 13. Mixing of interstitial fluid and ambient fluid quantified by the volumetric measure $V_{m,\theta}$ according to (5.3) at times $t = 0$, 20, 80, 200 and 1000. Same flow as in figure 2.

strongly increasing dependence of $V_{m,\theta}$ on the threshold value $c_{m,\theta}$ indicates that the inhomogeneities in the local concentrations of carrier fluid become more pronounced with time. Note that this inhomogeneity is also recognized from a visual examination of the marker field in figure 12, where at $t = 1000$ the marker distribution to the left appears much more sparse than to the right.

5.1. *Influence of settling velocity*

The vertical mixing of interstitial fluid and ambient fluid depends on both the amount of kinetic energy k in the fluid and the vertical stratification due to remaining particles which have not yet settled. Given that k continuously decreases after the start-up phase of the flow (see § 4), it can be expected that mixing will be reduced if the settling speed is reduced, since in this case the stabilizing density stratification is maintained for much longer times. To examine the influence of u_s on the mixing of ambient and interstitial fluid, figure 14 shows the marker distribution at $t = 1000$ of lock-exchange gravity currents with different settling velocities. In the density-driven case ($u_s = 0$), for which no sedimentation occurs, the heavy fluid containing the markers eventually collects in the neighbourhood of the bottom wall. Note that density-driven fronts have no final run-out length, and therefore the final thickness of this bottom layer of heavy fluid depends on the total length L_1 of the channel. In contrast, the propagation of particulate fronts comes to an end after all particles have sedimented and the difference in density, which drives the current, has vanished. However, as discussed in the previous section, fluid motion continuing beyond complete sedimentation causes ongoing mixing of fluid. From figure 14, it is recognized that the length of the region in which interstitial fluid is found decreases with increasing settling velocity, which reflects the fact that fronts with smaller u_s travel further downstream. On the other hand, the vertical mixing of carrier fluid and ambient fluid appears to be more uniform when the settling speed is higher. To assess the distribution of carrier fluid in the vertical direction, the concentration field is integrated over wall-parallel planes. This integral c_m^{i12} of the marker concentration over length and width of the channel

$$c_m^{i12}(x_3) \equiv \frac{1}{L_1^s L_2^s} \int_0^{L_2} \int_0^{L_1} c_m \, \mathrm{d}x_1 \, \mathrm{d}x_2, \tag{5.4}$$

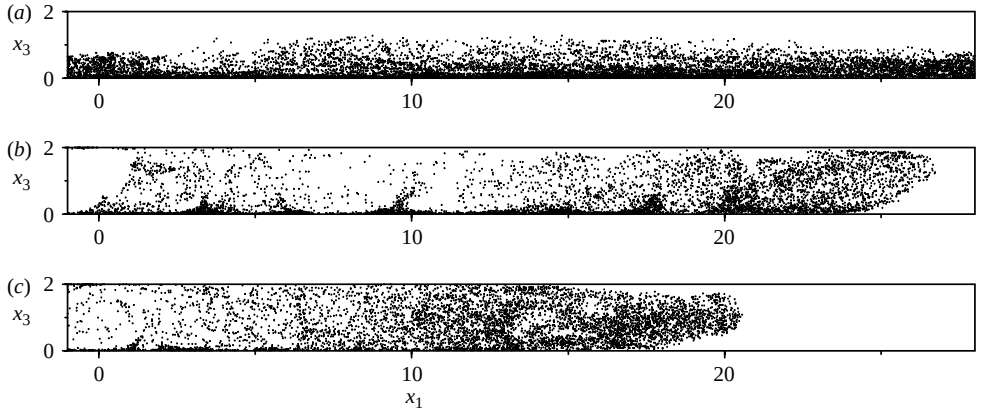

FIGURE 14. Mixing of interstitial fluid, visualized by passive markers. Results for time $t = 1000$. (*a*) Two-dimensional simulation of a density-driven flow ($u_s = 0$, $L_1 = 29$). (*b*) Three-dimensional simulation of a particle-driven flow with $u_s = 0.01$. (*c*) Particle-driven flow with $u_s = 0.02$ (same flow as in figure 2). Length and height of the initial reservoir, as well as the Grashof number, are identical in all simulations.

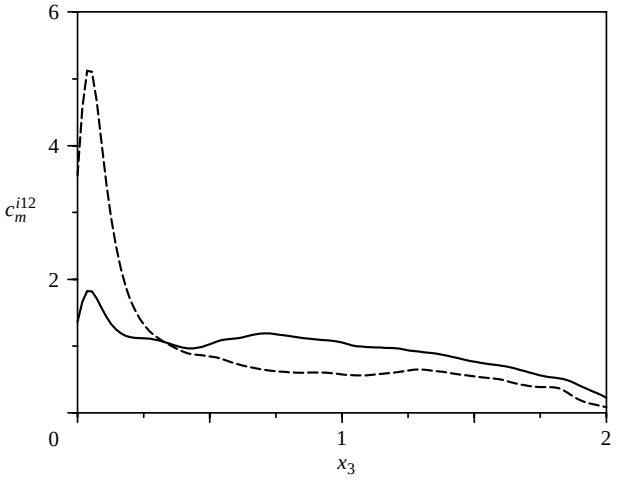

FIGURE 15. Vertical distribution of carrier fluid at time $t = 1000$ for $Gr = 5 \times 10^6$. c_m^{i12} represents the integral of c_m over the length and width of the channel according to (5.4). Solid line, same flow as in figure 2 ($u_s = 0.02$); dashed line, simulation with $u_s = 0.01$ (all other parameters identical).

is given in figure 15 as a function of the vertical coordinate at a time when the fluid has virtually come to rest. While in the case $u_s = 0.02$ (cf. figure 2) differences in the marker distribution between lower and upper channel half are relatively small, a strong asymmetry is seen in the curve for $u_s = 0.01$ with a pronounced peak near the lower wall, which can be inferred already from figure 14(*b*). The reason for these differences in the mixing behaviour for different settling speeds can be understood from a comparison of the respective results for the time history of kinetic energy k and the mass m_p of suspended material, given in figure 16. If we take the mass of suspended particles as an indicator for the stratification in the flow, m_p must have decreased sufficiently to allow for appreciable mixing in the vertical direction. Taking,

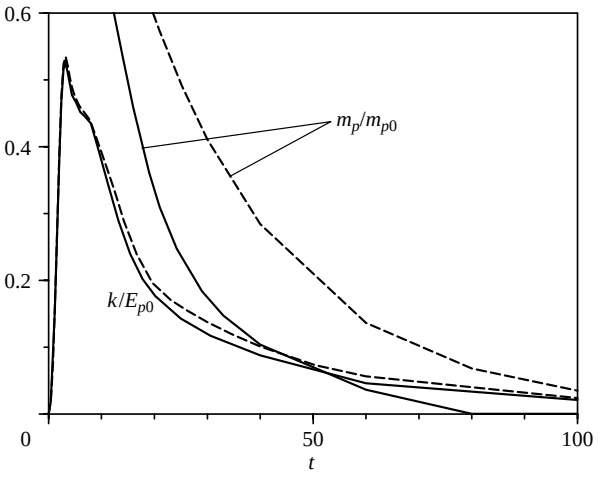

FIGURE 16. Temporal evolution of kinetic energy k, according to (4.4), and mass of suspended material m_p. Results normalized with the initial potential energy E_{p0} and the initial mass m_{p0}, respectively. Solid lines, same flow as in figure 2 ($u_s = 0.02$); dashed lines, simulation with $u_s = 0.01$ (all other parameters identical).

for example, $m_p/m_{p0} = 0.1$ as a rough guess for the limit below which stratification becomes insignificant, we find from figure 16 that enhanced mixing should be observed after about $t = 40$ and $t = 70$ for settling speeds of 0.02 and 0.01, respectively. However, the curves for $k(t)$ show that the remaining kinetic energy differs by a factor of two in these cases. Clearly, with more kinetic energy available, the mixing of interstitial and ambient fluid will be more intense. Note also that the extent of the region available for mixing is larger in the flow with smaller settling speed, owing to the increased run-out length of the front.

5.2. *Mixing in the deeply submerged case*

For the deeply submerged case, the mixing was also studied by the aid of passive markers. The distribution of the markers as a function of time can be seen from the side views depicted in figures 17 and 18 for early and late times, respectively. As for the lock-exchange flow, at early times the marker field resembles the shape of the propagating current. The pronounced head of the flow, as well as the almost undisturbed flow structure in the rear part, are clearly recognized from the marker distribution. The enhanced mixing at late stages, discussed before, sets in after $t = 40$, when most particles have settled and the stratification in the fluid has largely disappeared. At $t = 200$, markers are already distributed over a layer of thickness 3–4 times the height of the initial reservoir; at $t = 1000$, markers extend over the full channel height. At very late times, the vortices causing the mixing in the (x_1, x_3)-plane have grown to a length scale much larger than the channel width, leading to essentially two-dimensional motion. This is clearly recognized from the time history of the maximum vertical velocity and the maximum spanwise velocity depicted in figure 5 (note that both are normalized with the maximum streamwise velocity, which slowly decays with time). The structure of the large vortices is visualized in figure 18(d) by contours of the spanwise-averaged vorticity. We presume that the mixing in the very late stages of the flow is influenced by the narrow channel width, which favours large-scale two-dimensional motion; future simulations in much wider computational domains must show to what extent this affects the mixing properties of the flow.

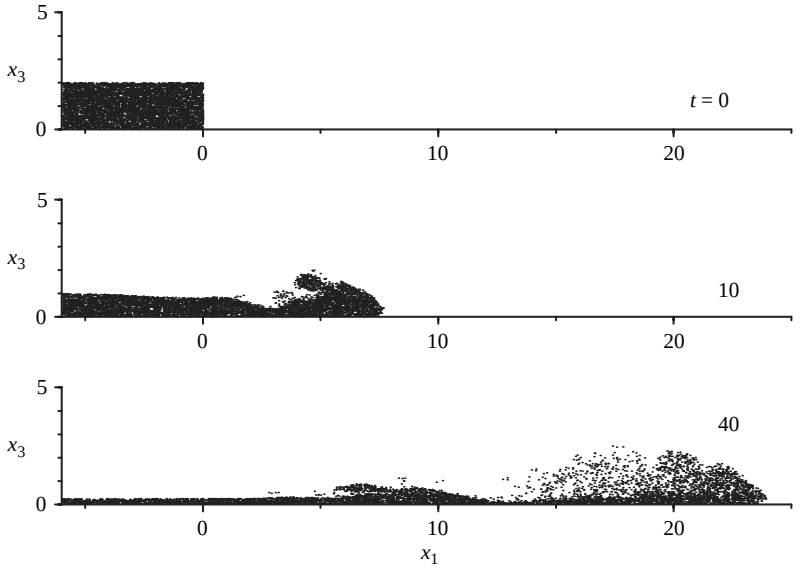

FIGURE 17. Dispersion of interstitial fluid in a deeply submerged flow for $Gr = 5 \times 10^6$ and $u_s = 0.02$, visualized by markers (early times).

6. Influence of initial turbulence

In the simulations presented so far, the fluid was generally at rest initially, except for the weak disturbances superimposed to enhance the breakdown of the flow at the leading edge. In practice, however, while the ambient fluid may be almost quiescent, the particle-laden fluid often is in turbulent motion at the onset of the gravity-driven flow. To examine the effect that such initial turbulence may have on the current, we performed two further three-dimensional lock-exchange simulations for the same geometry, Grashof number, and settling speed as the simulation shown in figure 2, but with turbulent disturbances superimposed to the fluid in the suspension reservoir. The kinetic energy k_0 contained in the flow at time $t = 0$ amounts to 12.5 % and 25 % of E_{p0}, respectively. In order to obtain a physically realistic turbulent velocity field, a separate simulation of decaying turbulence was conducted in a domain with the same dimensions as the reservoir. An impression of this initial turbulence field can be gained from figure 19, where a surface of the spanwise velocity component is depicted. To illustrate that the turbulence field has a broad range of excited scales in all three velocity components, we evaluated the following power density spectra of the flow

$$E_i(k_2) = \int_0^{L_1} \int_0^{L_3} |\hat{u}_i(x_1, k_2, x_3)|^2 \, \mathrm{d}x_3 \, \mathrm{d}x_1, \tag{6.1}$$

where $\hat{u}_i$ are the coefficients obtained from a spanwise Fourier transformation of the velocity fields, i.e. ($\mathrm{i} = \sqrt{-1}$, $\alpha_2 = \pi / L_2$)

$$f = \sum \hat{f}_k \, \exp(\mathrm{i}\alpha_2 k_2 x_2), \quad f = u_i. \tag{6.2}$$

The spectra are shown in figure 20. It can be seen that they exhibit a smooth decay over more than eight decades, from the large energy-containing structures to the dissipative scales.

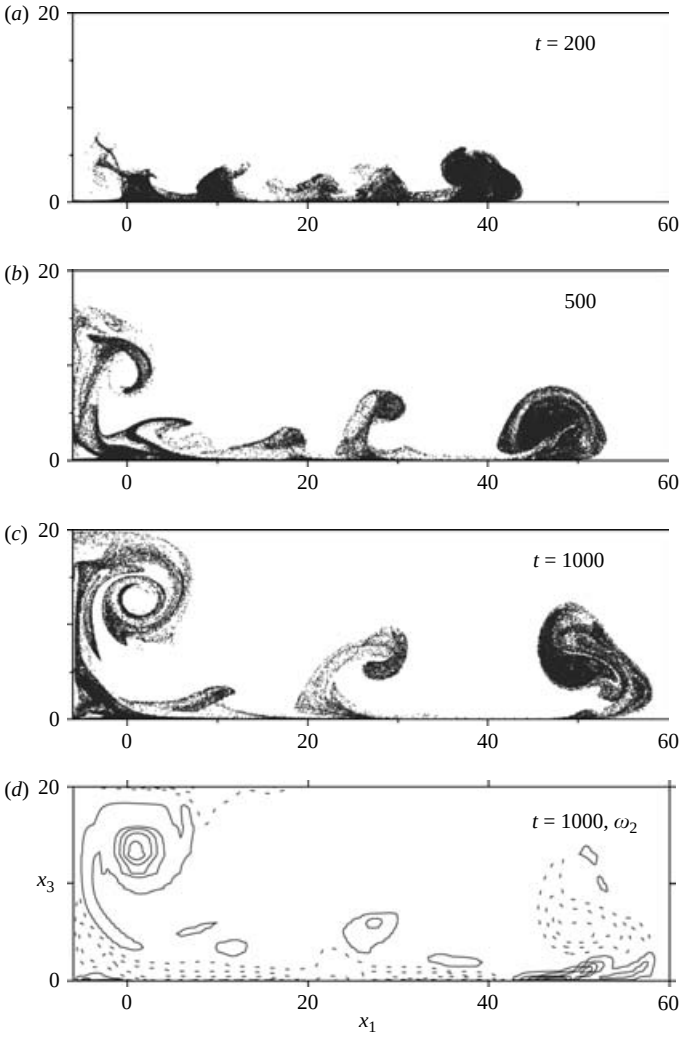

FIGURE 18. (*a*)–(*c*) Dispersion of interstitial fluid in a deeply submerged flow for $Gr = 5 \times 10^6$ and $u_s = 0.02$, visualized by passive markers (late times). (*d*) Spanwise-averaged vorticity component ω_2 at time $t = 1000$.

The most obvious effect of initial turbulence observed from our simulations, is that the mixing of the fluid within the current is strongly enhanced. To make this evident, we divide the passive markers initially added to the particle-laden fluid into 5 groups, stacked in the vertical direction (see the sketch in figure 21). During the propagation of the current, each group of markers is tracked individually. By displaying the instantaneous position of the markers of each of the five groups separately, the mixing within the carrier fluid can be assessed. Figure 22 gives the respective results for the simulation with $k_0 = 0.125 E_{p0}$, where markers are shown that were initially contained in the top, middle and bottom group. It can be seen that already at time $t = 8$, hardly any difference is discernible between the spatial distribution of markers originating from the different groups, showing that the suspension is well-mixed within the front. When comparing this result with figure 23, where the respective marker distribution is shown for the case $k_0 \approx 0.0$ (cf. figure 2), the strong enhancement of

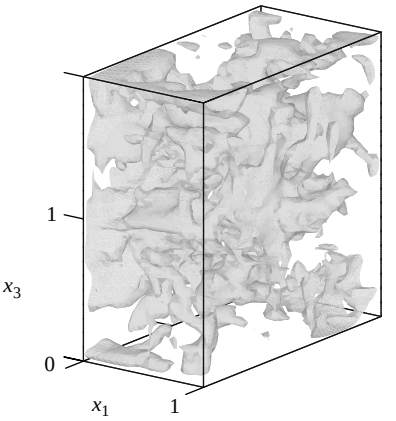

FIGURE 19. Initial turbulence field with a kinetic energy of $k_0 = 0.25E_{p0}$, visualized by a surface of spanwise velocity (isovalue set to 0.2).

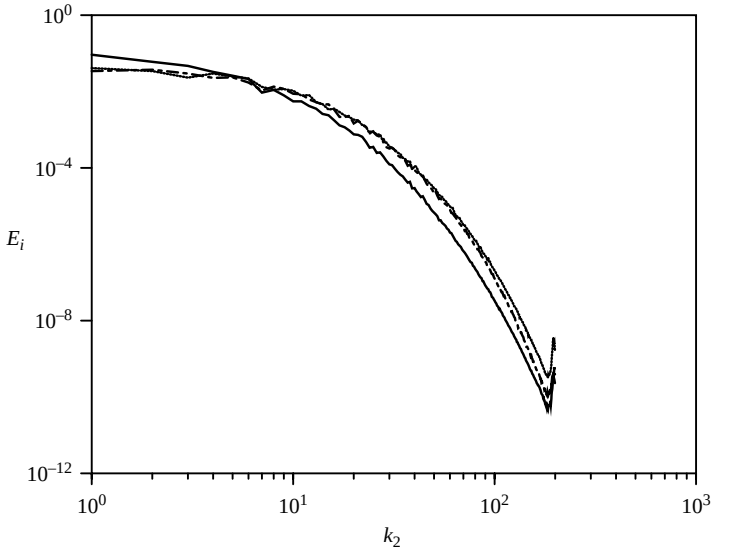

FIGURE 20. Spanwise modal energy (see (6.1)) of the turbulent flow shown in figure 19. E_1 (dot-dashed), E_2 (solid), E_3 (dotted).

internal mixing due to initial turbulence is obvious. Clearly, even in the case without initial turbulence, the fluid in the front is progressively mixed by developing turbulent motion, but on a slower time scale. It takes until about $t = 20$ before a thorough mixing within the front is observed in this case.

In contrast to the pronounced effect on the mixing within the front, figures 22 and 23 suggest that initial turbulence has only a minor influence on the overall flow development. A better impression of the differences in flow structure associated with different turbulence intensities is gained from figure 24, where, for all three simulations, contours of the spanwise-averaged concentration field are depicted at two selected times. It is seen that at $t = 10$, the flow structure is very similar, with some differences appearing only in the interfacial region. Here, a stronger initial turbulence field leads to an earlier breakdown of the coherent vortices, which are continuously shed from

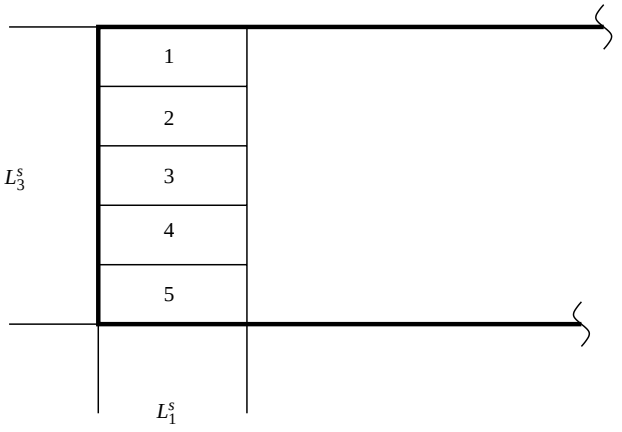

FIGURE 21. Subdivision of the initial volume of suspension into five subvolumes. The markers contained in each subvolume are considered as separate groups to examine the mixing within the front.

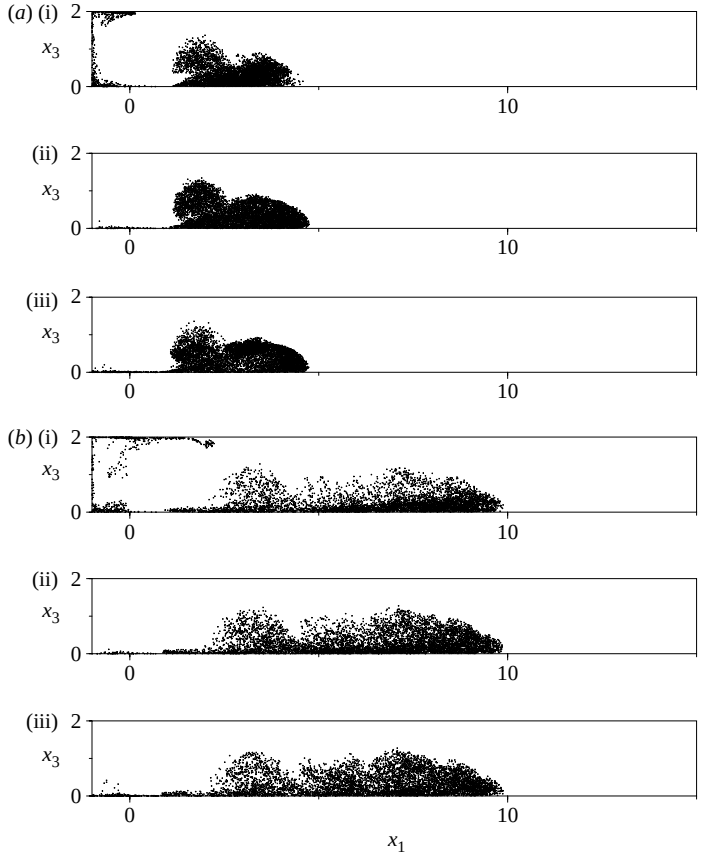

FIGURE 22. Distribution of passive markers illustrating the dispersion of interstitial fluid initially located in (i) subvolume 1, (ii) subvolume 3, and (iii) subvolume 5 (see figure 21). Results for the simulation with $k_0 = 0.125E_{p0}$, $Gr = 5 \times 10^6$ and $u_s = 0.02$. (*a*) $t = 8$, (*b*) 20.

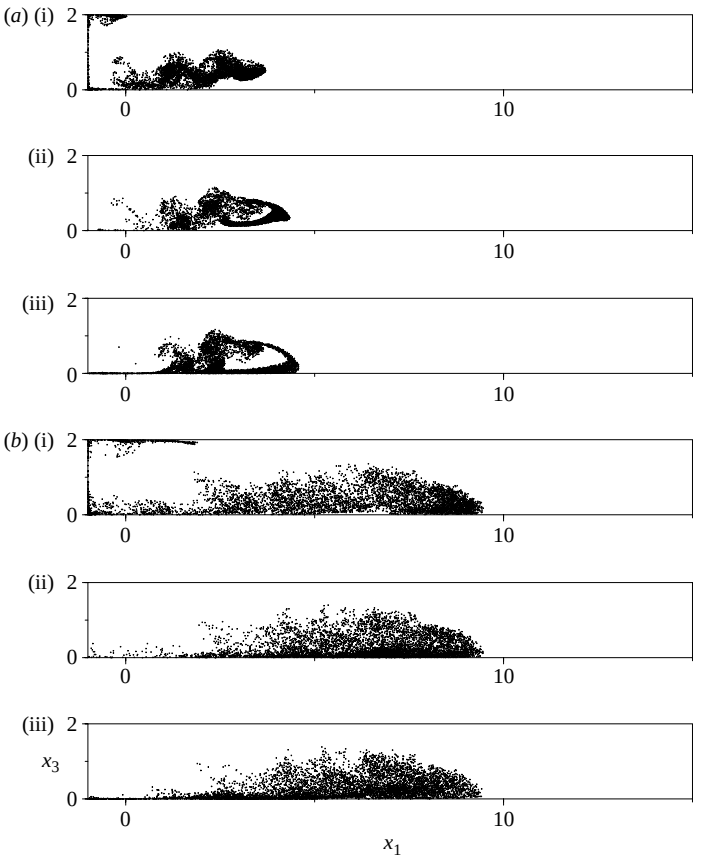

FIGURE 23. Distribution of passive markers illustrating the dispersion of interstitial fluid initially located in (i) subvolume 1, (ii) subvolume 3, and (iii) subvolume 5 (see figure 21). Same flow as in figure 2 ($k_0 \approx 0$). (*a*) $t = 8$, (*b*) 20.

the nose of the current. The differences become somewhat more pronounced only at later times, when the frontal velocities are slightly higher for higher k_0. These differences are better seen from figure 25, where the front position x_f and the mass of suspended material m_p are given as functions of time for the different cases. The curves for $x_f(t)$ essentially collapse at early times, but some deviations in the front position occur after $t \approx 15$. However, concerning $m_p(t)$, no appreciable effect of the initial turbulence level can be detected. All three curves are in very close agreement over the whole time interval between $t = 0$ and $t = 30$ for which direct comparison is made here.

The results presented in figures 24 and 25 demonstrate that the influence of the initial turbulence level within the suspension is weak, especially during the early flow development. This finding may seem surprising, since the difference between the three cases lies entirely in the initial conditions, which might suggest that the flow evolution immediately after the release should be affected more strongly than in the later stages. However, a closer look reveals that turbulent motion existing prior to the release is quickly damped by dissipation in the strongly accelerated flow during the formation of the front. To illustrate this, figure 26 compares the temporal evolution of potential energy, kinetic energy, and both dissipation components E_s and E_d as obtained from

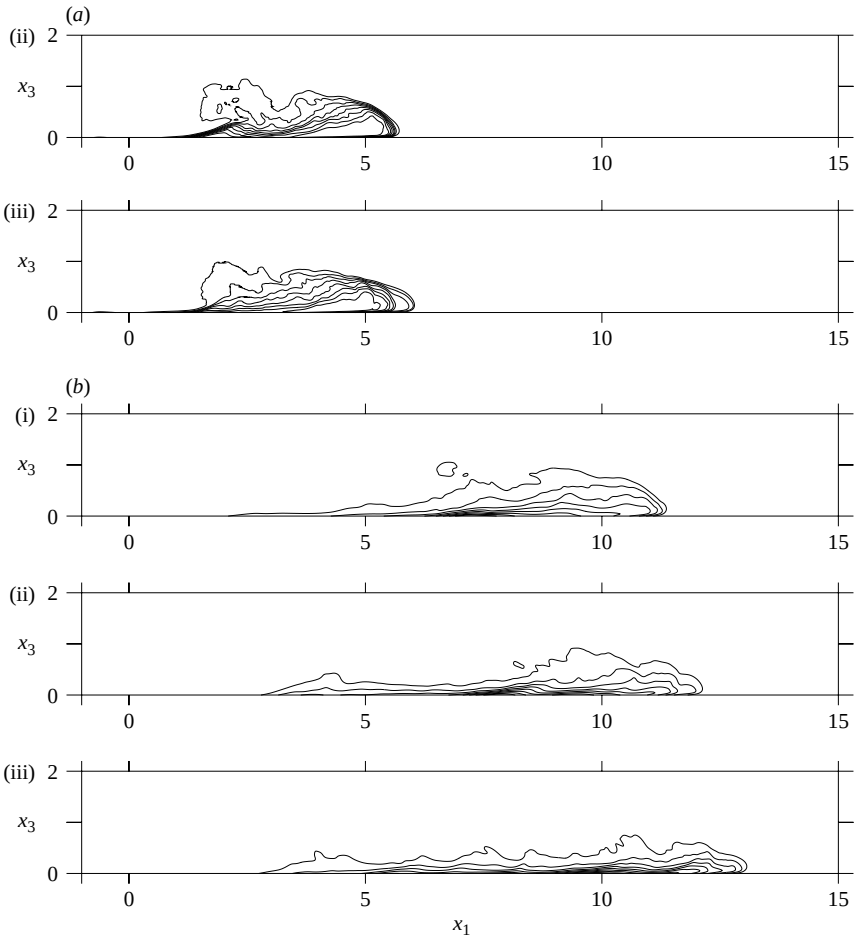

FIGURE 24. Contours of spanwise-averaged particle concentration at (*a*) $t = 10$, (*b*) $t = 30$. In all cases $u_s = 0.02$ and $Gr = 5 \times 10^6$. (i) $k_0 \approx 0$ (same flow as in figure 2), (ii) $k_0 = 0.125 E_{p0}$, (iii) $k_0 = 0.25 E_{p0}$.

the simulations with different initial turbulence levels. The differences with respect to k_0 are recognized from the values for k at $t = 0$. Note that the curves indicate that the initial kinetic energy in the turbulence field amounts to approximately 25 % and 50 % of the maximum kinetic energy in the later flow evolution, respectively. The initial differences in k, however, rapidly decrease within the first few time units owing to large dissipation rates (indicated by the strong increase of E_d in the simulations with $k_0 > 0$). The decay of the 'internal' turbulence is enhanced by the onset of the large-scale convective motion, which results in strong vortex stretching. We found the decay rate shortly after the release to be about twice as large as the decay rate observed in the preparatory simulation performed to generate the initial turbulence field. This large dissipation during the start-up phase of the gravity currents leads to offsets in the curves of E_d which amount to k_0 within an accuracy of a few per cent. The small differences between k_0 and this offset are again mainly due to the limited accuracy of the low-order scheme that was employed for the time integration required to compute E_d (cf. figure 7).

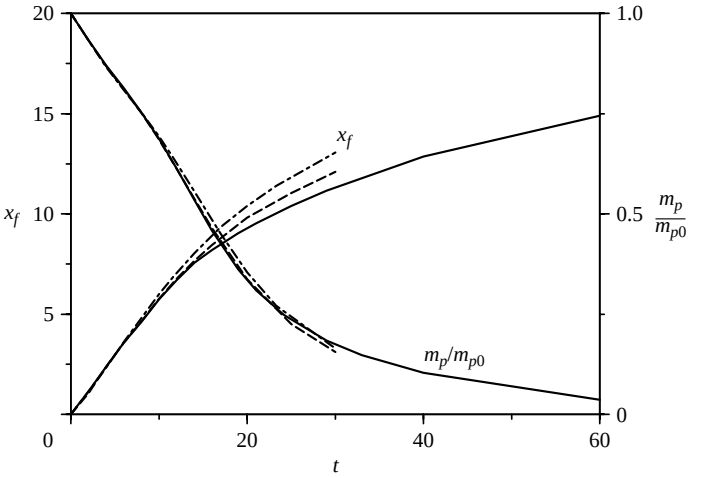

FIGURE 25. Front position x_f and mass m_p of suspended particles (normalized with the initial mass m_{p0}) as function of time for $Gr = 5 \times 10^6$ and $u_s = 0.02$. Comparison of results obtained from simulations with different initial turbulence levels. Solid line, same flow as in figure 2 ($k_0 \approx 0$); dashed line, $k_0 = 0.125 E_{p0}$; dot-dashed line, $k_0 = 0.25 E_{p0}$. (Simulations with $k_0 > 0$ were conducted until $t = 30$ only).

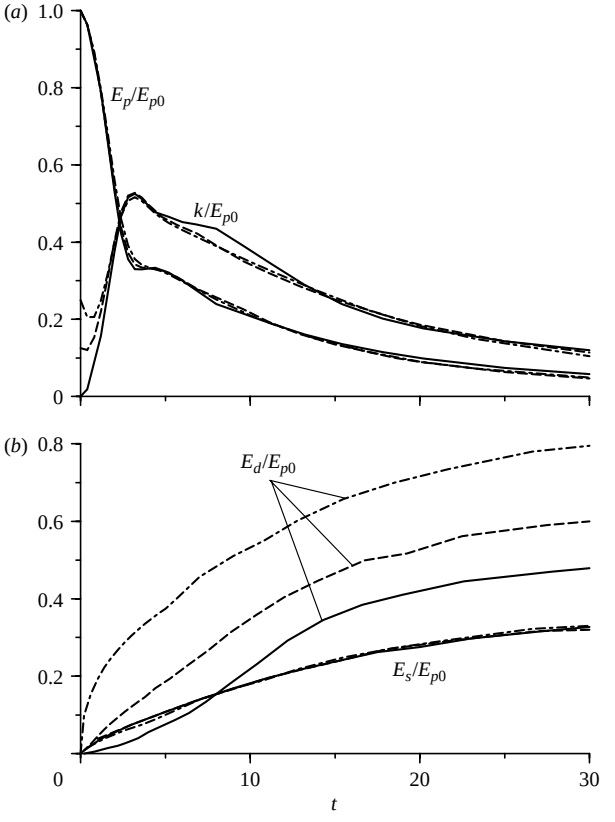

FIGURE 26. Time history of kinetic energy k, potential energy E_p and the dissipation components E_s and E_d, respectively (see (4.4), (4.5), (4.14), (4.15)) for $Gr = 5 \times 10^6$ and $u_s = 0.02$. Results normalized with the initial potential energy E_{p0}. Solid lines, same flow as in figure 2 ($k_0 \approx 0$); dashed lines, $k_0 = 0.125 E_{p0}$; dot-dashed lines, $k_0 = 0.25 E_{p0}$.

7. Summary

We have discussed results from a high-resolution computational study of particle-driven gravity currents developing either from a lock-exchange configuration or from a deeply submerged pool of suspension. The primary objective of the work was to analyse flow features that could not be studied in previous experimental or theoretical work. We have put special emphasis on the energy budget of the flow, showing how the conversion of potential energy into fluid motion and dissipative losses proceeds with time. Concerning the latter, we emphasized that in a particle-driven flow dissipation has two distinct components: one being due to gradients in the macroscopic convective velocity field, the other being caused by the microscopic Stokesian flow around each particle. The computational results suggest that, in a particulate front, both contribute about equally to the overall loss of mechanical energy. However, further simulations for a wider range of flow parameters may be required to clarify fully the generality of this finding.

Another flow feature addressed in detail is the mixing between ambient fluid and interstitial fluid. Both are assumed of equal density here, meaning that no stratification remains in the flow domain when all of the particles initially suspended have settled out. It was shown that after the propagation of the front has ceased, an enhanced mixing sets in that gradually spreads the interstitial fluid over the full channel height. How uniformly the interstitial fluid is eventually distributed depends, among other things, on the settling speed of the particles. The mixing is driven by large-scale vortices that persist after the particulate front has disappeared. For the deeply submerged flow, we observed that the vortices continually grow in diameter, tending to become two-dimensional. The influence that the width of the flow domain may have on this trend towards two-dimensionality is an aspect that deserves further analysis; however, computationally this issue can only be tackled at the expense of further greatly increased numerical effort.

E. M. gratefully acknowledges support of this research through NASA's Microgravity Program.

REFERENCES

Allen, J. R. L. 1971 Mixing at turbidity current heads, and its geological implications. *J. Sediment. Petrol.* **41**, 97–113.

Altinakar, S., Graf, W. H. & Hopfinger, E. J. 1990 Weakly depositing turbidity current on a small slope. *J. Hydaul. Res.* **28**, 55–79.

Beghin, P., Hopfinger, E. J. & Britter, R. E. 1981 Gravitational convection from instantaneous sources on inclined boundaries. *J. Fluid Mech.* **107**, 407–422.

Bonnecaze, R. T., Huppert, H. E. & Lister, J. R. 1993 Particle-driven gravity currents. *J. Fluid Mech.* **250**, 339–369.

Dade, W. B. & Huppert, H. E. 1994 Predicting the geometry of channelised deep-sea turbidites. *Geology* **22**, 645–648.

Dade, W. B. & Huppert, H. E. 1995 A box model for non-entraining, suspension-driven gravity surges on horizontal surfaces. *Sedimentology* **42**, 453–471.

Elghobashi, S. & Truesdell, G. C. 1993 On the two-way interaction between homogeneous turbulence and dispersed solid particles. I: Turbulence modification. *Phys. Fluids* A **5**, 1790–1801.

García, M. H. & Parsons, J. D. 1996 Mixing at the front of gravity currents. *Dyn. Atmos. Oceans* **24**, 197–205.

GLADSTONE, C., PHILLIPS, J. C. & SPARKS, R. S. J. 1998 Experiments on bidisperse, constant-volume gravity currents: propagation and sediment deposition. *Sedimentology* **45**, 833–843.

GLADSTONE, C. & WOODS, A. W. 2000 On the application of box models to particle-driven gravity currents. *J. Fluid Mech.* **416**, 187–195.

HÄRTEL, C. 2001 Model analysis of aspects of the flow field ahead of a density current. *Eur. J. Mech.* B/*Fluids* **20**, 415–425.

HÄRTEL, C., CARLSSON, F. & THUNBLOM, M. 2000*b* Analysis and direct numerical simulation of the flow at a gravity-current head. Part 2: The lobe-and-cleft instability. *J. Fluid Mech.* **418**, 213–229.

HÄRTEL, C., KLEISER, L., MICHAUD, M. & STEIN, C. F. 1997 A direct numerical simulation approach to the study of intrusion fronts. *J. Engng Maths* **32**, 103–120.

HÄRTEL, C., MEIBURG, E. & NECKER, F. 2000*a* Analysis and direct numerical simulation of the flow at a gravity-current head. Part 1. Flow topology and front speed for slip and no-slip boundaries. *J. Fluid Mech.* **418**, 189–212.

HALLWORTH, M. A., HUPPERT, H. E., PHILLIPS, J. C. & SPARKS, R. S. J. 1996 Entrainment into two-dimensional and axisymmetric turbulent gravity currents. *J. Fluid Mech.* **308**, 289–311.

HOGG, A. J., UNGARISH, M. & HUPPERT, H. E. 2000 Particle-driven gravity currents: asymptotic and box model solutions. *Eur. J. Mech.* B/*Fluids* **19**, 139–165.

HUPPERT, H. E. 1998 Quantitative modeling of granular suspension flows. *Phil. Trans. R. Soc. Lond.* A **356**, 2471–2496.

HUPPERT, H. E. & SIMPSON, J. E. 1980 The slumping of gravity currents. *J. Fluid Mech.* **99**, 785–799.

HUPPERT, H. E. 1986 The intrusion of fluid mechanics into geology. *J. Fluid Mech.* **173**, 557–594.

KNELLER, B. & BUCKEE, C. 2000 The structure and fluid mechanics of turbidity currents: a review of some recent studies and their geological implications. *Sedimentology* **47**, 62–94.

MAXEY, M. R., PATEL, B. K., CHANG, E. J. & WANG, L.-P. 1997 Simulations of dispersed turbulent multiphase flow. *Fluid Dyn. Res.* **20**, 143–156.

MAXWORTHY, T. 1999 The dynamics of sedimenting surface gravity currents. *J. Fluid Mech.* **392**, 27–44.

MEIBURG, E. 1995 Three-dimensional vortex dynamics simulations. In *Fluid vortices* (ed. S. Green), Kluwer.

MEIBURG, E., WALLNER, E., PAGELLA, A., RIAZ, A., HÄRTEL, C. & NECKER, F. 2000 Vorticity dynamics of dilute two-way coupled particle-laden mixing layers. *J. Fluid Mech.* **421**, 185–227.

MIDDLETON, G. V. 1993 Sediment deposition from turbidity currents. *Annu. Rev. Earth Planet. Sci.* **21**, 89–114.

MOHRIG, D., ELVERHØI, A. & PARKER, G. 1999 Experiments on the relative mobility of muddy subaqueous and subaerial debris flows, and their capacity to remobilize antecedent deposits. *Mar. Geol.* **154**, 117–129.

NECKER, F., HÄRTEL, C., KLEISER, L. & MEIBURG, E. 2002 High-resolution simulations of particle-driven gravity currents. *Intl J. Multiphase Flow* **28**, 279–300.

PARKER, G., FUKUSHIMA, Y. & PANTIN, H. M. 1986 Self-accelerating turbidity currents. *J. Fluid Mech.* **171**, 145–181.

DE ROOIJ, F. & DALZIEL, S. B. 1998 Time-resolved measurements of the deposition under turbidity currents. In *Proc. Conf. Sediment Transport and Deposition by Particulate Gravity Currents, Leeds, 7–9 September 1998.*

ROTTMAN, J. W. & SIMPSON, J. E. 1983 Gravity currents produced by instantaneous releases of a heavy fluid in a rectangular channel. *J. Fluid Mech.* **135**, 95–110.

SIMPSON, J. E. 1972 Effects of the lower boundary on the head of a gravity current. *J. Fluid Mech.* **53**, 759–768.

SIMPSON, J. E. 1997 *Gravity Currents in the Environment and the Laboratory*, 2nd edn. Cambridge University Press.

SPARKS, R. S. J., BONNECAZE, R. T., HUPPERT, H. E., LISTER, J. R., HALLWORTH, M. A., PHILLIPS, J. & MADER, H. 1993 Sediment-laden gravity currents with reversing buoyancy. *Earth Planet. Sci. Lett.* **114**, 243–257.

Thomas, N. H. & Simpson, J. E. 1985 Mixing of gravity currents in turbulent surroundings: laboratory studies and modelling implication. In *Proc. Conf. Models of Turbulence and Diffusion in Stably Stratified Regions of the Natural Environment, Cambridge, March 1983.*

Ungarish, M. & Huppert, H. E. 1998 The effects of rotation on axisymmetric particle-driven gravity currents. *J. Fluid Mech.* **362**, 17–51.

Ungarish, M. & Huppert, H. E. 2000 High-Reynolds-number gravity currents over a porous boundary: shallow-water solutions and box-model approximations. *J. Fluid Mech.* **418**, 1–23.

Winters, K. B., Lombard, P. N., Riley, J. J. & D'Asaro, E. A. 1995 Available potential energy and mixing in density-stratified fluids. *J. Fluid Mech.* **289**, 115–128.